

A Forecasting System of Computational Time of DFT/TDDFT Calculations under the Multiverse ansatz via Machine Learning and Cheminformatics

Shuo Ma,^{1,2} Yingjin Ma,^{1,3, a)} Baohua Zhang,^{1,3} Yingqi Tian,^{1,2} and Zhong Jin^{1,3, b)}

¹⁾*Computer Network Information Center, Chinese Academy of Sciences, Beijing 100190, China*

²⁾*School of Computer Science and Technology, University of Chinese Academy of Sciences, Beijing 101408, China*

³⁾*Center of Scientific Computing Applications & Research, Chinese Academy of Sciences, Beijing 100190, China*

(Dated: 19 October 2020)

A top-level designed forecasting system for predicting computational times of density-functional theory (DFT)/time-dependent density-functional theory (TDDFT) calculations is presented. The computational time is assumed as the intrinsic property for the molecule. Basing on this assumption, the forecasting system is established using the "reinforced concrete", which combines the cheminformatics, several machine-learning (ML) models, and the framework of many-world interpretation (MWI) in multiverse ansatz. Herein, the cheminformatics is used to recognize the topological structure of molecules, the ML/AI models are used to build the relationships between topology and computational cost, and the MWI framework is used to hold various combinations of DFT functionals and basis sets in DFT/TDDFT calculations. Calculated results of molecules from Drug-Bank dataset show that 1) it can give quantitative predictions of computational costs, typical mean relative errors can be less than 0.2 for DFT/TDDFT calculations with derivations of $\pm 25\%$ using the exactly pre-trained ML models, 2) it can also be employed to various combinations of DFT functional and basis set cases without exactly pre-trained ML models, while only slightly enlarge predicting errors.

^{a)}Electronic mail: yingjin.ma@sccas.cn

^{b)}Electronic mail: zjin@sccas.cn

I. INTRODUCTION

Ab initio electronic structure methods are becoming more and more popular in the chemistry community, as it has been reported that the *ab initio* methods illustrate the chemical mechanism in its original view, i.e., at the electron level¹⁻⁶. Normally, one needs to consider the computational costs of *ab initio* (i.e. first principle) methods when determining whether they are appropriate for the problem at hand or not. As shown in Fig.1, when compared to much less accurate approaches, such as molecular mechanics, *ab initio* methods often take larger amounts of computer time, memory, and disk space due to their scales. For example, the Hartree-Fock self-consistent field (HFSCF) and density functional theory (DFT) already shows scales in the range from $N^{2.x}$ to $N^{4.x}$ with N is the system magnitude parameters, not specifically the number of basis functions.^{7,8} The quantitative solutions (i.e. electronic correlation approaches) like Møller-Plesset perturbation theory up to 2nd order (MP2)⁹, coupled cluster approaches with single and double excitations (CCSD)^{10,11} and iterative perturbed treatment (CCSD(T)) increase the scales by two or more orders, respectively. Comparing to HF approach, DFT, MP2, and CCSD/CCSD(T) perfectly include dynamic correlations where it fails is in taking static correlations, i.e. quasi-degeneracy. The quasi-degeneracy is normally accounted by the multi-configurational and multi-reference approaches,¹² and their scales can be in a large range due to the so-called active space, in which the super-position of all possible configurations can be took into account for describing the quasi-degeneracy.^{8,12}

Normally, one needs to choose the simulating approaches carefully by considering the studied systems as well as the desired accuracy. Apparently, the choice of simulating approaches, or even the choice of parameters in a given approach is also dominated by the computational resources.⁸ However, the predictable pace of Moore’s law¹³ cannot easily compensate for the difficulties caused by the conflict between computational resources and computational scales. Thus, there are actual demands for predicting the possible computational costs (e.g. time, memory, or disk space) before performing the simulations. It can benefit both researchers and computer centers in terms of computational resource utilization and computational resource scheduling, respectively.¹⁴

Several related works have been carried out in the area of computational cost modelling and job scheduling in the past decades. Most of the related works chose to make

use of historical data and adopt methods of statistical analysis and machine learning (ML), with which the relationship between job features and the computational cost can be established.^{15–26} One of the research prospects was characterized by laying emphasis on the meta information of jobs, including user types, number of processors applied for, execution time limits and so on. These works took the assumption that different jobs with similar meta information come with similar costs, which was validated by Downey¹⁵ and Smith’s¹⁶ works. Time series approaches have been frequently used in this kind of works. For instance, Gaussier *et al.*¹⁸ designed a feature set including varieties of job history data as the input of a linear regression model. Moreover, many works focused on the the architectures of the targeted systems and use ML to make predictions. The training

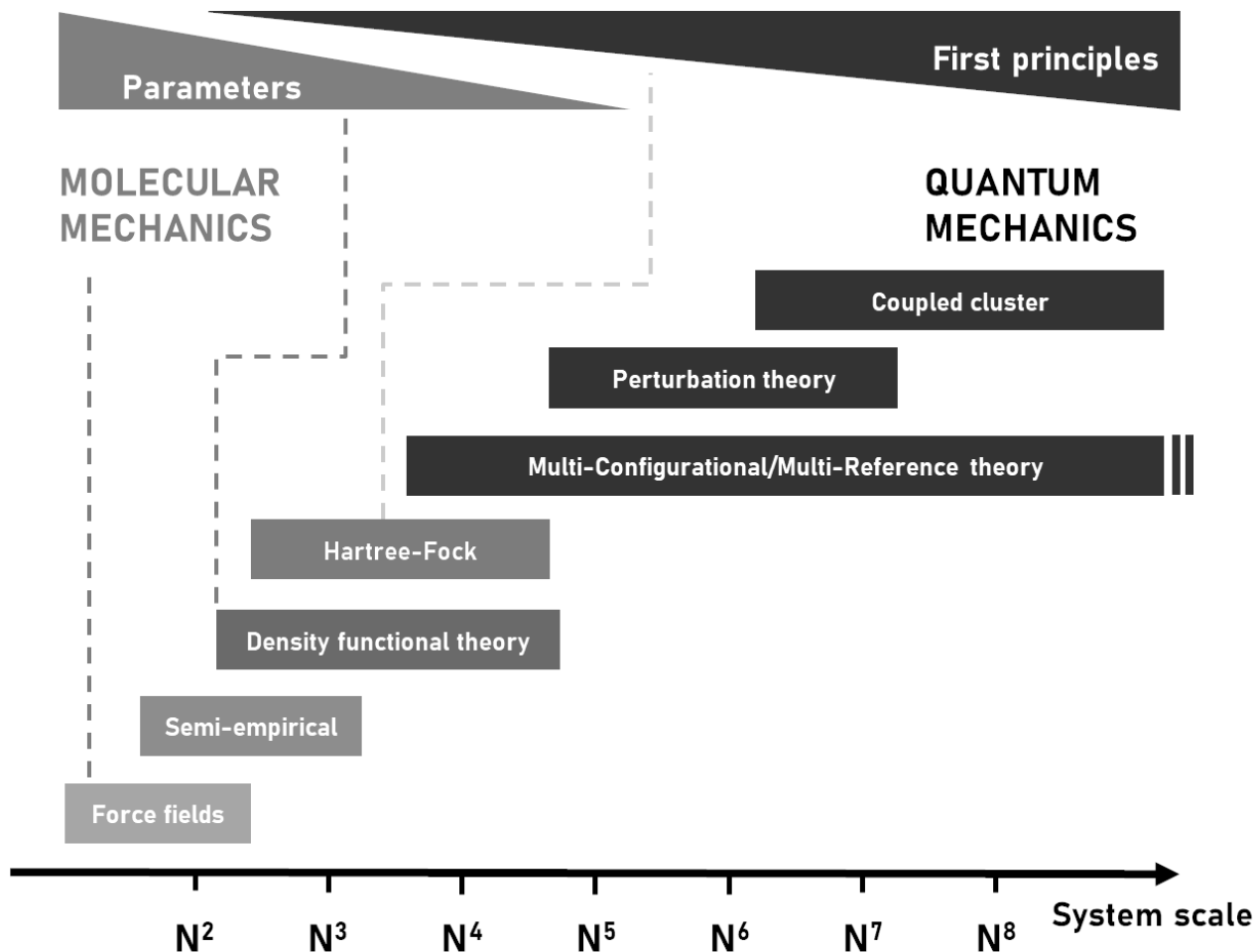


FIG. 1. The system scales under different simulating approaches.

data usually come from hardware performance counters so that the states of computing components during executions can be considered. Li *et al.*²⁰ used a support vector machine (SVM) model to predict the instruction number in each cycle and obtain the optimal thread mapping scheme. Helmy *et al.*²² employed SVM, artificial neural network, and decision tree models to predict CPU burst time, and it can be further extended to a heterogeneous computing system as shown by Shulga *et al.*²³. Apart from the above solutions targeting common programs, there are also some predictive methods specified for a certain type of programs.^{24,25} It is worthy of note that Matsunaga *et al.*²⁶ applied the PQR2 model to predict the execution time, memory, and disk occupations of two bioinformatics applications (BLAST²⁷ and RAxML²⁸). It has been reported that taking features that were highly correlated with application types, such as protein sequence length, yields much better results.

Regarding to the field of computational chemistry, Papay *et al.* developed a least square fitting method for graph-based component-wise runtime estimates in parallel SCF atomic computations in 1996.²⁹ Antony *et al.* used a linear model to simulate the runtime of SCF algorithms in Gaussian applications and to estimate the impacts of architectures in terms of the count of retired instructions and cache misses.³⁰ Additionally, it is noteworthy that Mniszewski *et al.* designed a class of tools for predicting the runtime of a molecular dynamics code,³¹ allowing users to find the optimal combination of algorithmic methods and hardware options. However, as far as we know, there is nearly no related work concerning to the prediction of computation cost in the field of quantum chemistry, except in the area of quantum machine learning (QML) models that very recently introduced by Heinen and coworkers.¹⁴ They demonstrated that QML-based wall time predictions significantly improve job scheduling efficiency by reducing CPU time overhead ranging from 10% to 90%. Until now, there is no universal solution for predicting the computational cost. The current QML solution is restricted to a specified computational approach and specified parameters, and training of a corresponding ML model is essential before practical predictions.¹⁴ However, it may not be convenient for training the specific model each time before the practical calculations. Thus, generalization ability should be one of the essential elements for an universal solution when predicting the computational cost. Additionally, the traditional ML models including the ensemble learning³², recurrent³³ or graph-based neural network³⁴, may also be the good

alternatives to the reported QML solutions.¹⁴

Herein, a top-level design-based forecasting framework is developed, which aims to yield reliable prediction of computational cost (mainly the computational time) with a high degree of generalization ability. At this stage, we focus on its design and its confirmatory usage via the prediction of computational times of DFT/TDDFT single-point calculation. In our design, cheminformatics is used to recognize the topological structure of molecules, and the ML models are used to establish the relation between topology and computational time. Additionally, the idea from many-world interpretation (MWI) in multiverse ansatz is used to gain generalization ability when treating with various combinations of DFT functional and basis sets, which are critical for practical calculations.^{35–37}

For the DFT calculations, the computational scaling is range from $N^{2.x}$ to $N^{4.x}$, as shown in Fig.1 and detailed explained in appendix. It stems from the evaluation of four-center two-electron repulsion integrals, i.e.,

$$(\mu\nu|\lambda\sigma) = \int \int \phi_\mu(1)\phi_\nu(1)\frac{1}{r_{12}}\phi_\lambda(2)\phi_\sigma(2)d\tau_1d\tau_2, \quad (1)$$

where μ, ν, λ , and σ denote indices of atomic orbitals. This scaling is the upper boundary for the HF or DFT calculations.^{38,39} However, many two-electron integrals are of negligible magnitude for large molecules, and some rigorous upper boundary conditions can be applied to the integrals. For instance, the Schwarz inequality⁴⁰

$$|(\mu\nu|\lambda\sigma)| \leq \sqrt{(\mu\nu|\mu\nu)(\lambda\sigma|\lambda\sigma)} \quad (2)$$

can reduce the mathematical upper bounds of all two-electron integrals to be computed in an $N^2 \log N$ process by safely ignoring the predetermined negligible integrals. Additionally, larger molecular systems have a higher fraction of atomic orbitals sufficiently distant from each other to be considered non-interacting, thereby yielding negligible two-electron integrals and further decline the exponent for HF or DFT calculations.³⁸

It was demonstrated by Strout and Scuseria that the number of basis functions n can connect with the integrals via the scaling exponent α for the same molecular series,³⁸ e.g.

$$\left(\frac{n_2}{n_1}\right)^\alpha = \left(\frac{I_2}{I_1}\right), \quad (3)$$

where n denotes the number of basis functions and I denotes the number of integrals. Because the computational cost of integrals are the upper boundary for the HF or DFT

calculations, such that a $t = an^2 + bn + c$ type formula (exponent 2 is roughly approximated from α) can be expected as the working equation for rough prediction the time. However, the simple polynomial equation or the exponential expression (Eq.3) is only suitable for the molecules in the same series and better without significant scale difference. When molecules have different spatial structures, the predicted results are normally too poor to be referred when using this type of regression equation.³⁸ Additionally, it is not convenient for this regression analysis to consider multiple factors (e.g., basis number together with electrons, bond type, etc.), which should be considered when better predictions are needed. Thus, the advantages of the proposed top-level design-based forecasting framework can be demonstrated in practical predictions.

The paper is organized as follows: in Sec. II, we present the design of the proposed framework, implementation details, and the workflow of the forecasting system; computational details presented in Sec. III while benchmark examples are presented in Sec. IV; and finally, we draw the conclusions of the work in Sec. V.

II. IMPLEMENTATIONS

A. Chemical spaces containing the computational times

Chemical space is a concept in cheminformatics referring to the property space, which is spanned by all possible molecules adhering to a given set of construction principles and boundary conditions.^{41–45} As shown in Fig.2, the chemical space considered in this work is spanned by possible molecules and their computational times, which are treated as the intrinsic properties of molecules. Different computational schemes (e.g. hardware, software, and approaches, etc) lead to different computational times for molecule. Thus, there are various chemical spaces for a given set of molecular suits. Even when a specific approach is employed, there are still various chemical spaces that are generated by the parameters. For instance, different choices of DFT functionals, basis sets, quantum chemical packages etc. can generate different chemical spaces, even if the same DFT approach is employed.

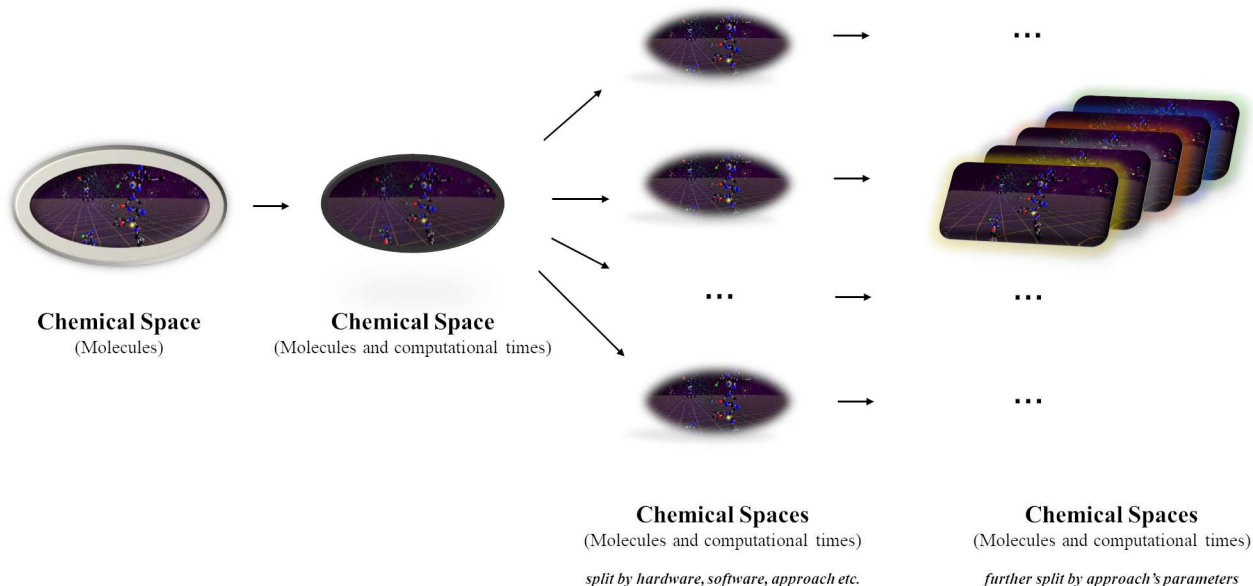


FIG. 2. The illustration of chemical spaces that contain molecular suits and computational times. The chemical spaces can be split by different computational schemes (e.g. hardware, software, and approaches, etc), and can be further split by approach’s parameters. The figure was captured from CSV tool developed by Probst and Reymond.⁴⁶

B. Cheminformatics and the employed ML/AI models

As mentioned previously that the proposed DFT chemical spaces can be further split by different computational parameters, hence, ML techniques can be employed in each split chemical space, to train the models that can be used to perform predictions. In each DFT chemical space, we employed several ML models, from simple to complex, to benchmark their capacities and correspondingly to pick up the reliable framework for predicting the computational times. There are four carefully selected ML models within this framework, they are as follows:

1) Random Forest (RF),^{47,48} basing on the structural similarity. The composition proportion of a molecule respecting to the feature structures (e.g. linear, dendritic, ring, etc.) can be evaluated by the decision trees constructed by the designed feature structures via the smiles molecular input line entry specification (SMILES) codes.^{49–51} Then the predicted computational time can be estimated by a linear combinations of computational times of feature structures. The idea behind this process is quite similar to the linear combination of atomic orbitals (LCAO) approximation in quantum chemistry.

2) Long Short-Term Memory (LSTM),^{52,53} basing on the recognition of chemical for-

mula. The connection between molecular structures and computational times is recognized by training the similar molecular suits. The molecular structures are identified via the SMILES codes using the natural language processing (NLP),⁵⁴ and the bidirectional variation of LSTM model^{55–57} is practically implemented in this work.

3) Message Passing Neural Network (MPNN),⁵⁸ basing on the graph-based learning of spatial structures. The connection between molecular structures and computational times is recognized by training the similar molecular suits using their spatial informations. The number of basis functions, number of electrons, bond types, molecular charges etc. can be considered as a whole in this model.

4) Multilevel Graph Convolutional Neural network (MGCN),⁵⁹ similar to MPNN, has advantages in the terms of generalizability and transferability.

The brief procedure is also shown in Fig.3. There are more details of these four ML models in appendix section, which can be referred for the interested readers.

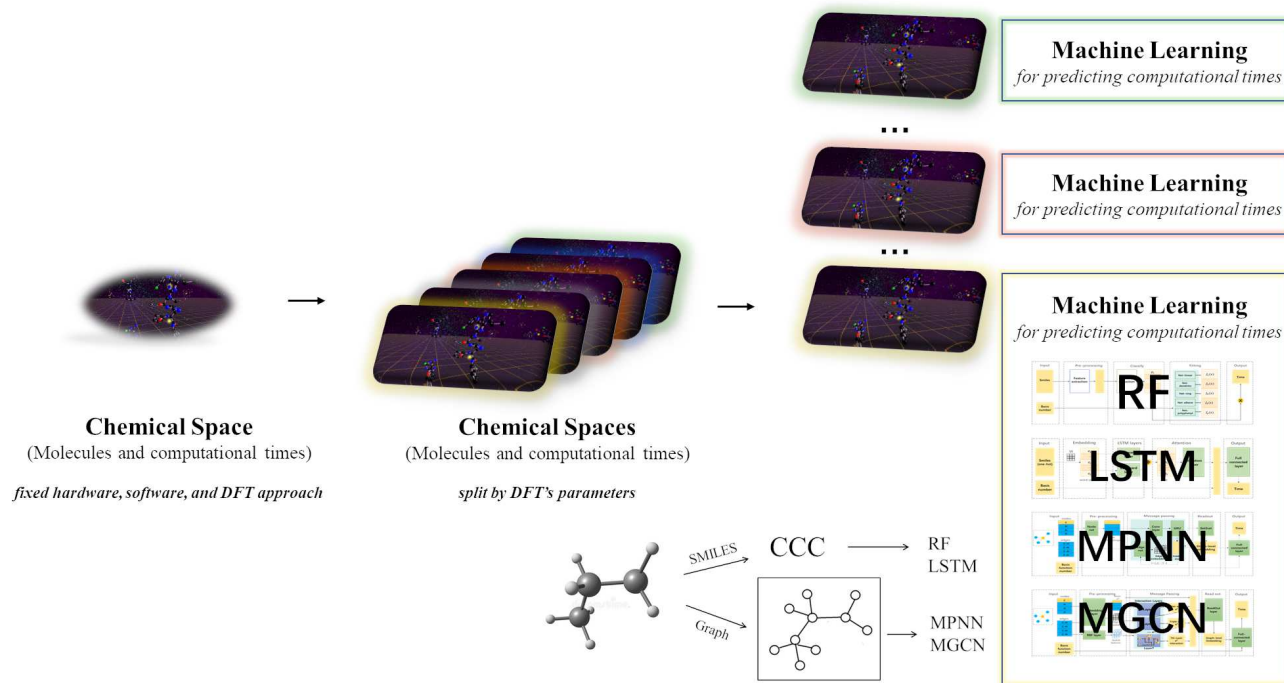


FIG. 3. Illustration of DFT chemical space, and the chemical spaces split by the computational parameters (e.g. DFT functionals, basis sets). ML techniques are employed for the purpose of predicting computational times.

C. Chemical MWI ansatz and the generalization

The chemical MWI ansatz used in this paper is inspired by Hugh Everett III’s MWI multiverse ansatz,^{60–64} in which there is an interpretation of quantum mechanics that asserts that the universal wave function is objectively real, and that there is no wave function collapse. It implies that all possible outcomes of quantum measurements are physically realized in some “world” or “universe”, and they all share a unique start point. As shown in Fig.3, in chemical MWI ansatz, the **unique start point** can be the chemical space, in which the same molecular suits and Kohn-Sham working equation are deployed, and every **result’s world** is the split chemical space caused by the uneven DFT parameters, which in turn result in different wave functions and different computational times as the intrinsic properties for the same molecular suits of the start point. As illustrated in the Fig.4.

It is worthy of note that the molecular suits are included in the start point and shared by all split chemical spaces, thus, the relationships between the computational times among various split chemical spaces can be connected by the molecular suits. In the original MWI, the status of cat (i.e. observed object) in one space can always be determined/deduced by the status of cat in the other space via the so-called quantum entanglement^{67,68}. In the chemical MWI of this work, we assume the computational times (i.e. observed objects) in one space can also be deduced by the computational times in other spaces via fitting relationships. The fitting relationships can be deduced by the molecular suits or just some molecules in the suits. As shown in Fig.5, these molecules are defined as the joint molecules, since they represent the joints for various split chemical spaces, and can connect these split chemical spaces through the molecular link and the link surface (surface implies that it contains the computational properties like computational times).

Herein, it worth mentioning that the fitting relationships obtained via one or few molecular links may be generalized to the split chemical spaces if the solving manner for the KS equation is fixed. And as such, the computational times within split chemical spaces, which are caused by various combinations of basis set and DFT functional, can be well considered within this ansatz. For DFT functionals, the correction coefficients of computational times for split chemical space can be approximated by the molecular link, and the Jacob’s ladder^{36,69} may be used as the entry point for further classify the func-

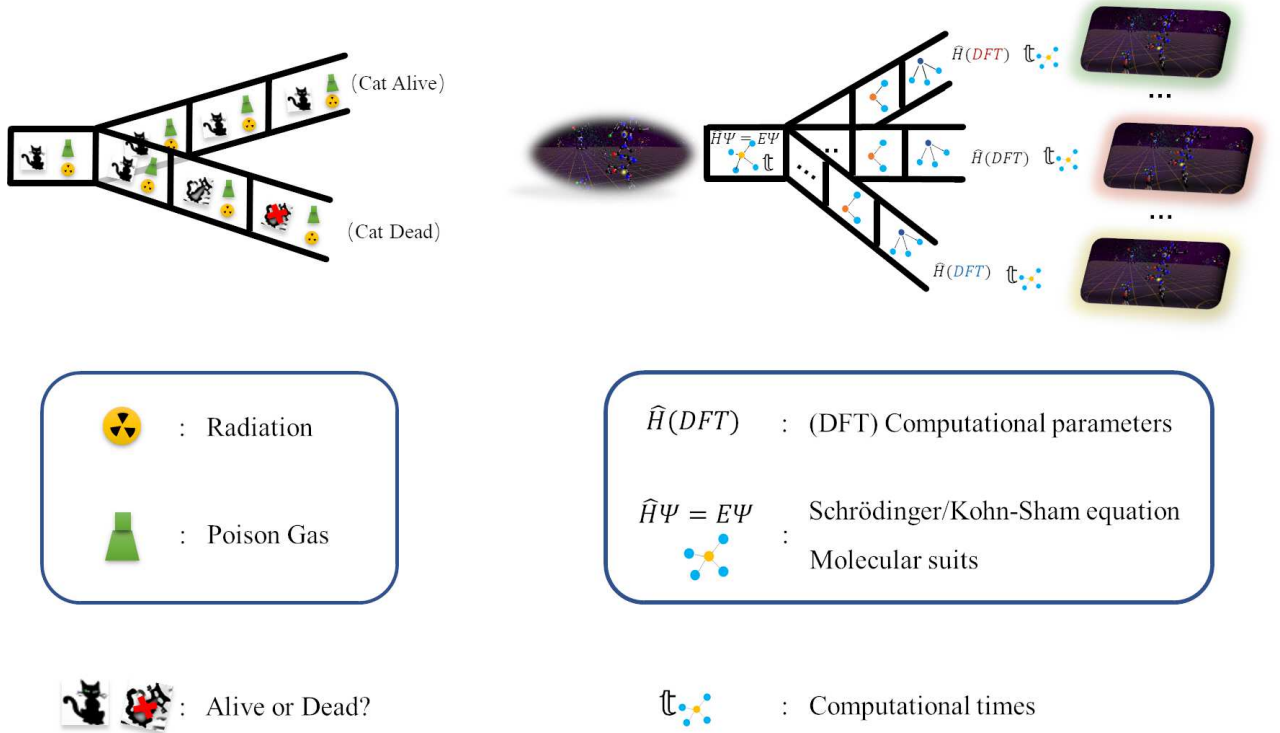


FIG. 4. Comparative illustration of original MWI using "Schrödinger's cat" paradox^{65,66} and chemical MWI ansatz used in predicting the computational times in this work. In the MWI ansatz, every quantum event is a branch point; the cat is both alive and dead, even before the box is opened, but the "alive" and "dead" cats are in different branches of the universe, both of which are equally real and depended on "Radiation? \rightarrow Poison Gas \rightarrow Cat status" process, but do not interact with each other. In the chemical MWI ansatz, different branches are split by the computational parameters that affect the actual implementation/solution of Hamiltonian operators (\hat{H}) following the "Parameters \rightarrow KS equation & molecule \rightarrow Computational times" process.

tionals that did not occurred in link surface. In this case, the correction coefficient for the target DFT functional under the specific basis can be obtained from the expression

$$c^{dft} = f^{dft}(tar) / f^{dft}(ref), \quad (4)$$

in which the $f^{dft}(tar)$ and $f^{dft}(ref)$ are the target and reference timing data, respectively, for the molecular link. If the $f^{dft}(tar)$ is not available, the DFT functional within the same region of Jacob's ladder can be used as the substitution. For basis sets, the correction

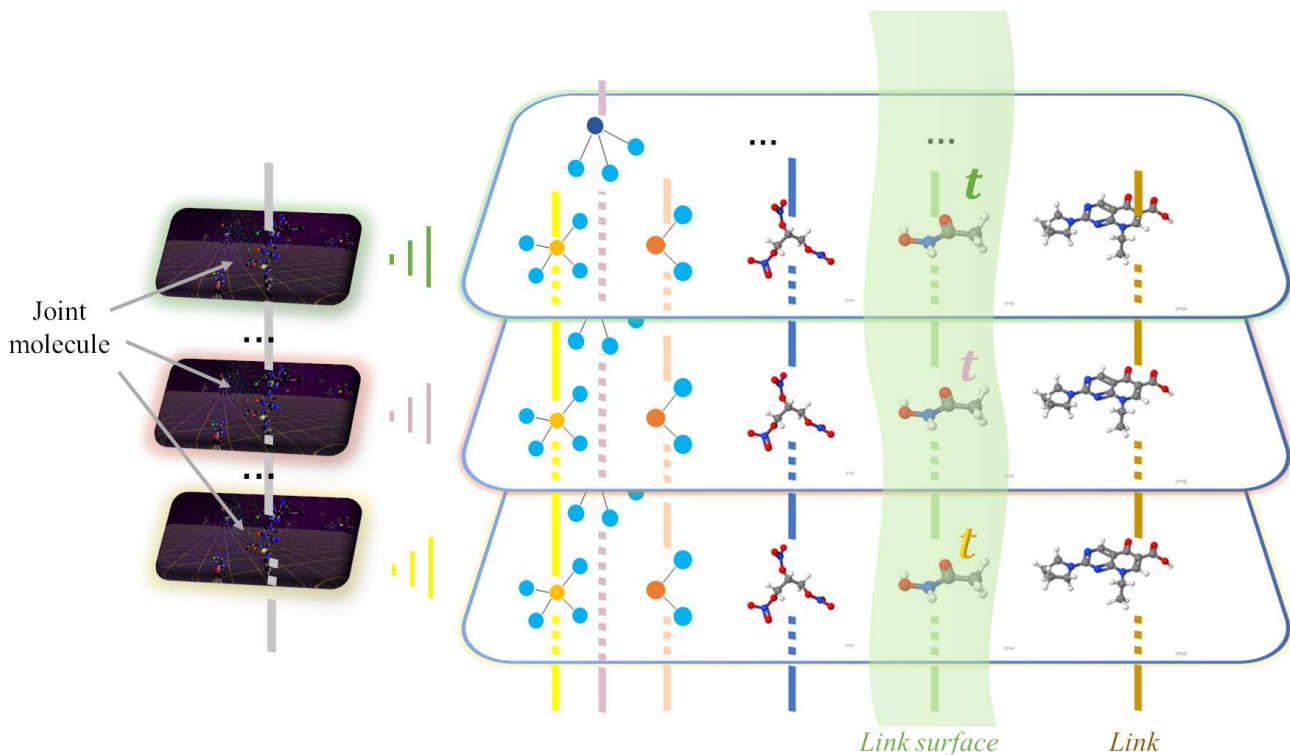


FIG. 5. Illustration of split chemical spaces, molecular link via joint molecule, and link surface used in the chemical MWI.

coefficients can be approximated by the molecular link via a polynomial curve-fitting technique. In this case, the correction coefficient for the target basis set under the specific DFT functional can be obtained through the expression

$$c^{bas} = f^{bas}(x_{tar}) / f^{bas}(x_{ref}), \quad (5)$$

in which the $f(x)$ denotes the fitted polynomial equation using various basis sets under the specific DFT functional, and x denotes the number of basis functions. If the second-order polynomial is used, then

$$f^{bas}(x) = ax^2 + bx + c \quad (6)$$

can be used for calculating the timing data for the target and reference basis sets, respectively. Nevertheless, it is worthy of note that the reliability of the correction coefficient is affected by the deviation of target basis set and reference basis set. Here, a similarity coefficient is introduced as a measurement of the deviation between the target and reference

basis sets. The formula of similarity coefficient (s) can be expressed as

$$s = \frac{\min(N_{tar}, N_{ref})}{\max(N_{tar}, N_{ref})} \cdot (1 - |\rho_{tar} - \rho_{ref}|) \cdot J, \quad (7)$$

where $N_{tar/ref}$ represents the number of atomic basis functions, ρ measures the contractions of basis sets,

$$\rho = \frac{N_{pri}}{N_{con}} \quad (8)$$

with N_{pri} representing the number of primitive basis functions and N_{con} represents the total number of contracted basis functions, and J denotes the Jaccard index⁷⁰⁻⁷² reflecting the similarity of orbital composition of the two basis sets. Further,

$$J = \frac{r}{r + p} \quad (9)$$

where r represents the number of identical atomic basis functions between the target and reference basis sets, p represents the number of atomic basis functions in either of them. The closer that s is to 1, the closer the two basis sets are.

D. Forecasting System

Fig.6 shows the workflow of our proposed forecasting system. For any input molecule, the forecasting system can have the capacity to give a predicted DFT computational time for a specific hardware, software with any combination of DFT functional and basis sets.

III. COMPUTATIONAL DETAILS

We used the BASIS SET EXCHANGE,⁷³ a community database for quantum chemistry electronic structure calculations to obtain the information of basis sets and electrons. The STK⁷⁴ package together with the RDKit⁷⁵ package were used for generating the molecular suites. These two packages were also used for extracting and labeling properties of the molecular suites. All the calculations were implemented by the GAUSSIAN⁷⁶, NWChem⁷⁷, GAMESS⁷⁸, or OPENMOLCAS⁷⁹ packages. The self-written scripts using PYTHON with NUMPY, and PYTORCH⁸⁰ were used for automatic execution of the calculations, assembling the data, and analyzing the results.

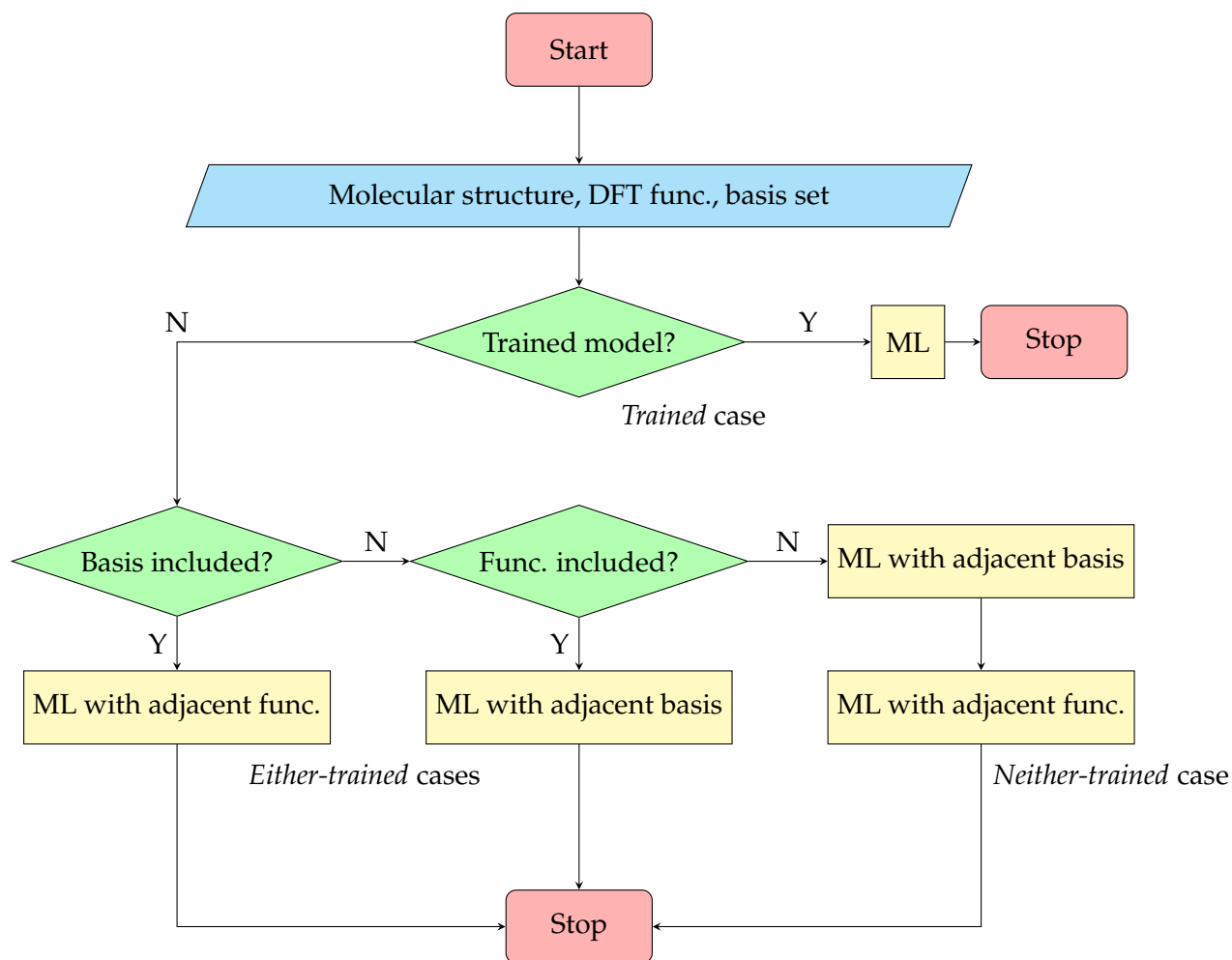


FIG. 6. Workflow of the proposed forecasting system.

The molecular suit of the RF with FNN model was artificially designed, containing 108 molecules with typical structures. When training the models, five typical molecular suits (i.e. single/double-bond linear, branch, ring, and polyphenyl) were used as the training suits for RF models. The molecular suit of Bi-LSTM, MPNN, and MGCN models were sampled from the DrugBank dataset.^{81–83}. The criteria applied to select the molecules for the training and test sets from DrugBank dataset were as following:

- a. divide all molecules of DrugBank into groups basing on the rows of periodic table of elements, manually select the desired groups (e.g. groups that contains the first two rows elements) to form the molecular suits.
- b. further divide the selected molecular suits into sub-groups basing on the number of atoms without the H atom.

c. randomly select the training molecules and testing molecules in each sub-groups with fixed ratio (e.g. 4:1) to form the training reservoir and testing reservoir.

d. choose the appropriate number of molecules from the training/testing reservoir to form the training/testing suits that in practical usages.

When training the models, the width of the hidden layers was set to five meaning that every hidden layer has five neurons. The mean absolute error (MAE) loss,

$$MAE = \frac{1}{N} \sum_{i=1}^N |\hat{y}^{(i)} - y^{(i)}| \quad (10)$$

was used as the target function, and the mean relative error (MRE),

$$MRE = \frac{1}{N} \sum_{i=1}^N \frac{|\hat{y}^{(i)} - y^{(i)}|}{y^{(i)}} \quad (11)$$

was used for evaluating the performance of the model. For an input sample i , the $\hat{y}^{(i)}$ denotes the model output and the $y^{(i)}$ denotes the real value of the prediction target. Adam optimizer⁸⁴ was used in minimizing the loss.

IV. RESULTS AND DISCUSSIONS

A. Predicting with pre-trained models

At the beginning, the ML models in foresting system were evaluated, to assess their capacity of distinguishing of molecules. Several molecules, which have nearly the same total number of basis functions but with different geometrical configurations, were used for illustrations. As shown in Fig.7, there are 25 sample molecules that are grouped into 5 rows: A-row and B-row are the molecules from the RF training suits, and C-, D-, and E-row are the molecules randomly selected from the DrugBank database. The molecules in the same column own almost the same total number of basis functions but different geometrical configurations when using the 6-31G basis sets⁸⁵ with M06-2x DFT functional⁸⁶.

Fig.7 presents the predicted total CPU time, CPU time averaged to each SCF iteration, and their relative errors. It can be seen that the predicted total CPU times using LSTM models show the best accuracy, and the calculated MRE of testing 25 molecules is about 0.13 (Tab.I). The results of MPNN, MGCN models also show relatively good accuracy with MRE values were 0.17 and 0.21, respectively. The results of RF shows the poorest

results with MRE is 0.37. It can also be observed in Fig.7 that a similar tendency can be observed for the averaged CPU times. To evaluate the capacity of the proposed method in identifying molecules with different size, the MRE values of total CPU times for column grouped molecules with different sizes were also listed in Tab.I. A decreasing accuracy was observed in LSTM \rightarrow MPNN \rightarrow MGCN \rightarrow RF order. Except the RF model, both LSTM and MPNN/MGCN models can give the reliable predictions for each column’s molecules. It implied that these three models had the capacities to consider the changes of computational times that caused by the structural differences.

TABLE I. The MRE values of total computational times for testing molecular suits and grouped molecules (shown in) with different number of basis functions.

Model	Testing suit (25 samples)	Col-1	Col-2	Col-3	Col-4	Col-5
RF	0.37	0.89	0.29	0.06	0.23	0.36
LSTM	0.13	0.12	0.10	0.11	0.15	0.15
MPNN	0.17	0.17	0.06	0.16	0.16	0.27
MGCN	0.21	0.25	0.16	0.17	0.25	0.24

After evaluating the classification capacities of the models in the proposed foresting system, we further checked how the magnitudes of the training suits affect the accuracy. Because the training suits in the RF models were fixed and artificially designed, the other three models (i.e. LSTM, MPNN and MGCN) were checked in this part by increasing or decreasing the molecules in the training suits. Herein, the starting point of the training suits only includes four typical molecular suits that were used in the RF models, then the molecules from the DRUGBANK database were gradually added. The testing suit contained 116 molecules that extracted from the DrugBank database. The results were shown in Fig.8. It can be seen that the MRE values of testing suits can already attain lower than 0.2 value for all these three ML models with less than 1000 molecules in the training suits. This magnitude of training suits was far less than that the one obtained in image recognition, because the SMILES or one-hot representations of chemical elements can already recognize the constituent of molecules. Thus only the geometric constructions need to be learned when training the models.

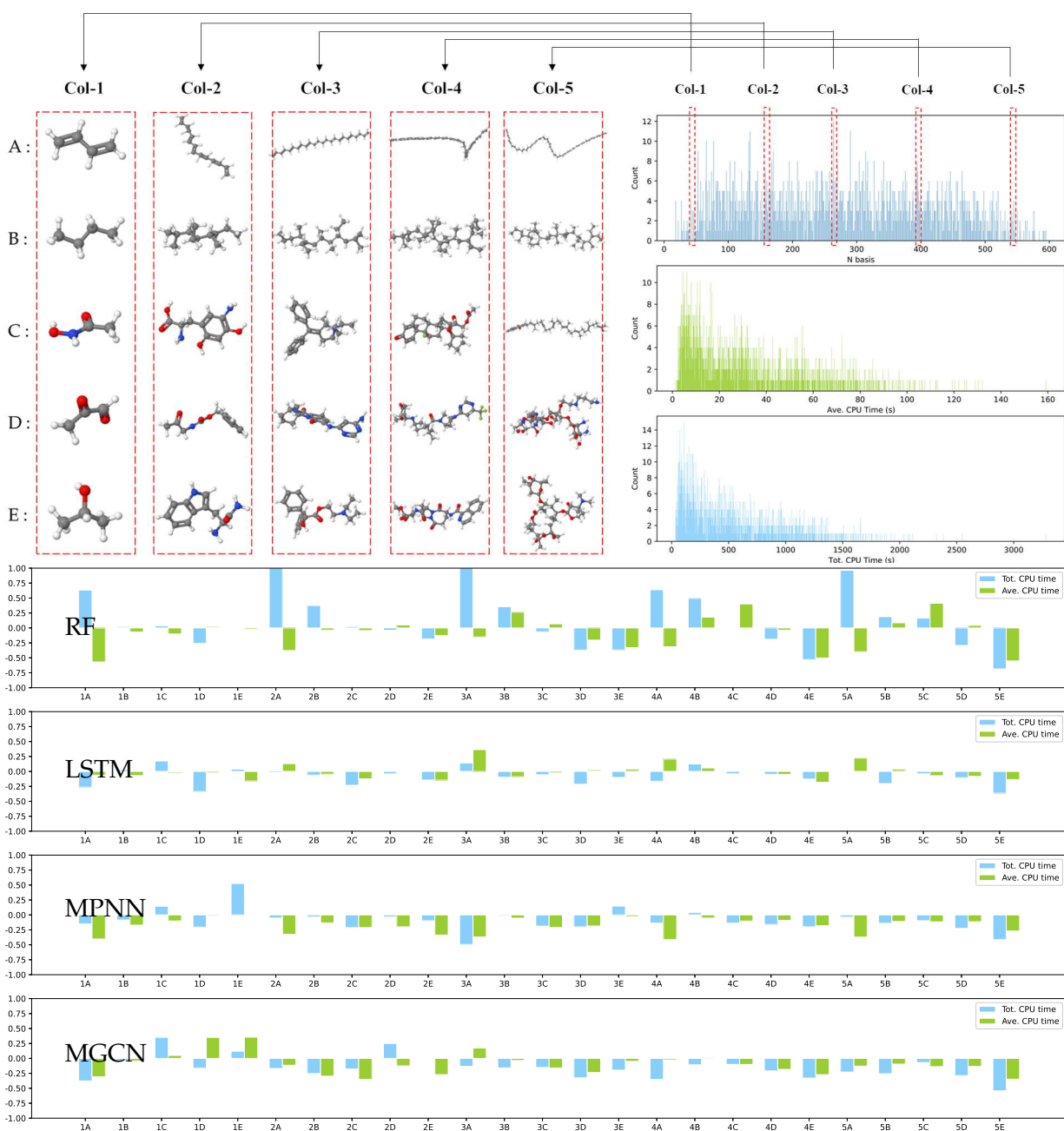


FIG. 7. **Top left** : Illustration of sampled geometrical configurations of testing molecules. A-row and B-row are the molecules from the RF training suits, while C-, D-, and E-row are the molecules randomly selected from the DRUGBANK database. The molecules in the same column possess almost the same total number of basis sets but different geometrical configurations when using the 6-31G basis sets. **Top right** : The distributions of the total number of basis functions and the CPU times for all the molecule suits, as well as the positions of the sampled molecules. **Bottom** : The relative errors of the predicted CPU time for all the sampled molecules.

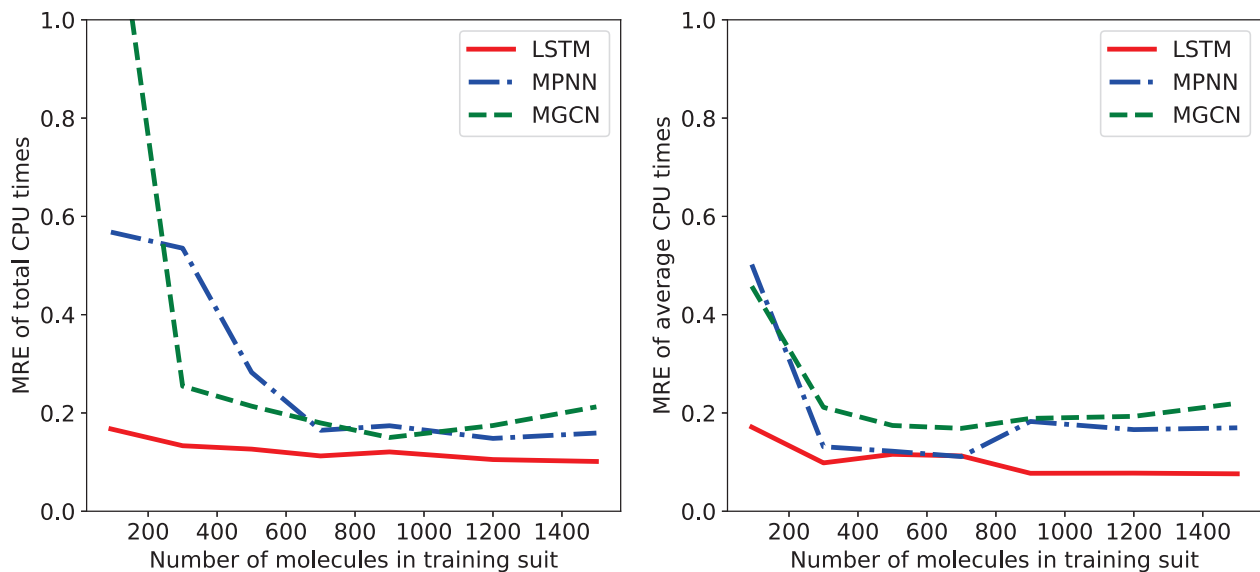


FIG. 8. Illustrations of the MRE of testing molecules for total/average CPU times along with the the total number of molecules in the training suits.

Assuming that one has the typical aiming molecules, e.g., PE molecules or drug molecules, then there may be ways for optimizing the training of the ML models using a fewer number of training suits, or to achieve higher accuracies. Here, we propose "space-specific" (S.-S.) and "space-averaged" (S.-A.) ways for training the models. In the former case, only the molecules of the same type as the aiming molecules were selected to the training suits. However, in the latter case, several types of molecules were used to ensure better generalization ability. For demonstration purposes, molecules of the PE suits (as part of molecules shown in row-A of Fig.7), branch suits (as part of molecules shown in row-B of Fig.7) and the DrugBank suits (as part of molecules shown in row-C, D, E of Fig.7) were used as the training and testing suits. The results for the LSTM, MPNN, and MGCN models were shown in Tab.II. It can be seen that the MREs of LSTM models for both S.-S. and S.-A. cases were quite close to each other, the derivations were normally less than 0.04 for both total and averaged CPU times. For the graph-based MPNN and MGCN models, the MREs of S.-S. case were in general larger than those of the S.-A. case in the small case, e.g., total CPU results of MPNN's branch (MRE was 0.63) and Drug-Bank/M100 (M100 denotes 100 training molecules, with MRE was 0.42,) and MGCN's DrugBank/M100 (MRE was 0.31). However, the MREs can be reduced by simply adding the number of training samples, e.g., in the total CPU results for the MPNN/MGCN's DrugBank/M300-700 cases, the MREs were reduced to around 0.15. This was line with

the tendency shown in Fig.8 that a certain amount of samples were needed for graph-based models. Overall, there was no obvious difference between S.-S. and S.-A. strategy when enough training samples were used (e.g. $M > 300$), and a decreasing accuracy was observed in LSTM \rightarrow MGCN \rightarrow MPNN \rightarrow RF order.

TABLE II. The MREs of predicted total CPU times and predicted averaged CPU times for each iteration (in bracket) of the ML models using space-specific and space-averaged training approaches.

Model	Training manner	PE	Branch	Drug			
				(M=100)	(M=300)	(M=500)	(M=700)
LSTM	S.-S.	0.13 (0.05)	0.11 (0.09)	0.12 (0.13)	0.09 (0.12)	0.10 (0.12)	0.10 (0.13)
	S.-A.	0.15 (0.07)	0.06 (0.05)	0.13 (0.13)	0.11 (0.11)	0.14 (0.19)	0.11 (0.10)
MPNN	S.-S.	0.17 (0.11)	0.63 (0.12)	0.42 (0.19)	0.16 (0.15)	0.15 (0.15)	0.13 (0.14)
	S.-A.	0.21 (0.27)	0.20 (0.12)	0.21 (0.19)	0.16 (0.13)	0.16 (0.17)	0.20 (0.13)
MGCN	S.-S.	0.14 (0.06)	0.11 (0.09)	0.31 (0.12)	0.20 (0.10)	0.12 (0.10)	0.15 (0.11)
	S.-A.	0.18 (0.09)	0.14 (0.16)	0.16 (0.10)	0.15 (0.11)	0.12 (0.15)	0.14 (0.15)

To check the predictions for various DFT/TDDFT calculations, different combinations of popular DFT functionals ("PBE"⁸⁷, "BLYP"^{88,89}, "bhandhlyp"⁹⁰, "B3LYP"⁹¹, "LC-BLYP"⁹², "CAM-B3LYP"⁹³, "M06"⁸⁶, "M062x"⁸⁶, " ω B97XD"⁹⁴) and Pople's basis sets ("6-31G", "6-31G*", "6-31+G*")⁸⁵ were used for this purpose. The results for the total/average CPU times of ground state DFT calculations, and total CPU times of singlet excited state TDDFT calculations, respectively, were illustrated in Fig.9. The S.-S training approach was used in these calculations with 1000 training molecules and the selected 116 testing molecules. Overall, it can be concluded that MGCN \sim LSTM $>$ MPNN $>$ RF in terms of overall performance. To be specific, in the case of predicting total CPU times of ground state DFT calculations (Fig.9), all the four models showed good predicting capacities when using 6-31G basis sets with MREs around 0.10, while the MREs increased when polarization and diffused functions were added. For instance, the average MREs of RF model even turned to about 0.51 for the 6-31+G* case, and 0.30 for the MPNN case. Meanwhile, the MGCN and LSTM can still guarantee reliable predictions with MREs around 0.17. The results of MGCN showed better stability than those of the LSTM, it may have benefited from the graph-based learning approach of MGCN, in which the na-

ture of its convergence manner (e.g. total iterations) can also be implicitly integrated in learning of the total CPU times. A similar tendency ($\text{MGCN} \sim \text{LSTM} > \text{MPNN} > \text{RF}$) was observed for the prediction of total CPU times of singlet excited state TDDFT calculations with lightly augmented MRE values for all these models. Apart from the MREs for the predictions, the scattered error distributions were also illustrated in Fig.10 for the M06-2x functional with these three basis sets. It can be seen that the MGCN and LSTM show good stability when most scatters were located in the $\pm 25\%$ regions, regardless of the predictions of ground or excited states.

Before the end of this subsection, the NWChem, GAMESS, and MOLCAS packages were interfaced with the forecasting system using the same four models, to check the predicting capacity for the general quantum chemical package. The calculated MRE results are shown in Fig.11. It can be noticed that all the benchmarked packages basically resemble with each other when using the same ML models. The LSTM and MGCN models still showed the best precision for predictions, and thus, can be deployed in the forecasting system as the working models.

B. Predicting without pre-trained models

All the aforementioned ML models were trained in the given chemical space, now we continue to show how the forecasting system give the predictions without using pre-trained models (i.e., either-trained or neither-trained models) of the given chemical space using the chemical WMI anastz. As we mentioned in section II-C, a plethora of different combinations of DFT functional/basis set could be the main obstacle for general forecasting. Thus, it is necessary to benchmark how the DFT functionals and basis sets play their roles in the practical calculations, separately. Herein, the relation between CPU times and parameters of DFT functionals or basis sets were shown in Fig.12 and Fig.13, respectively, via the sampled link molecule (i.e. simple CH_3CONHOH as shown in Fig.5).

Fig.12 shows the ratios between CPU times of various functionals and those of PBE functional were evaluated for the DFT functionals. It can be seen that the variations of DFT functionals did not change the CPU times a lot, e.g. the average magnifications of CPU time were in the range of 0.90 to 1.2. Furthermore, the increase of various DFT functionals can be roughly assigned to four regions referred to as the Jacob ladder. For

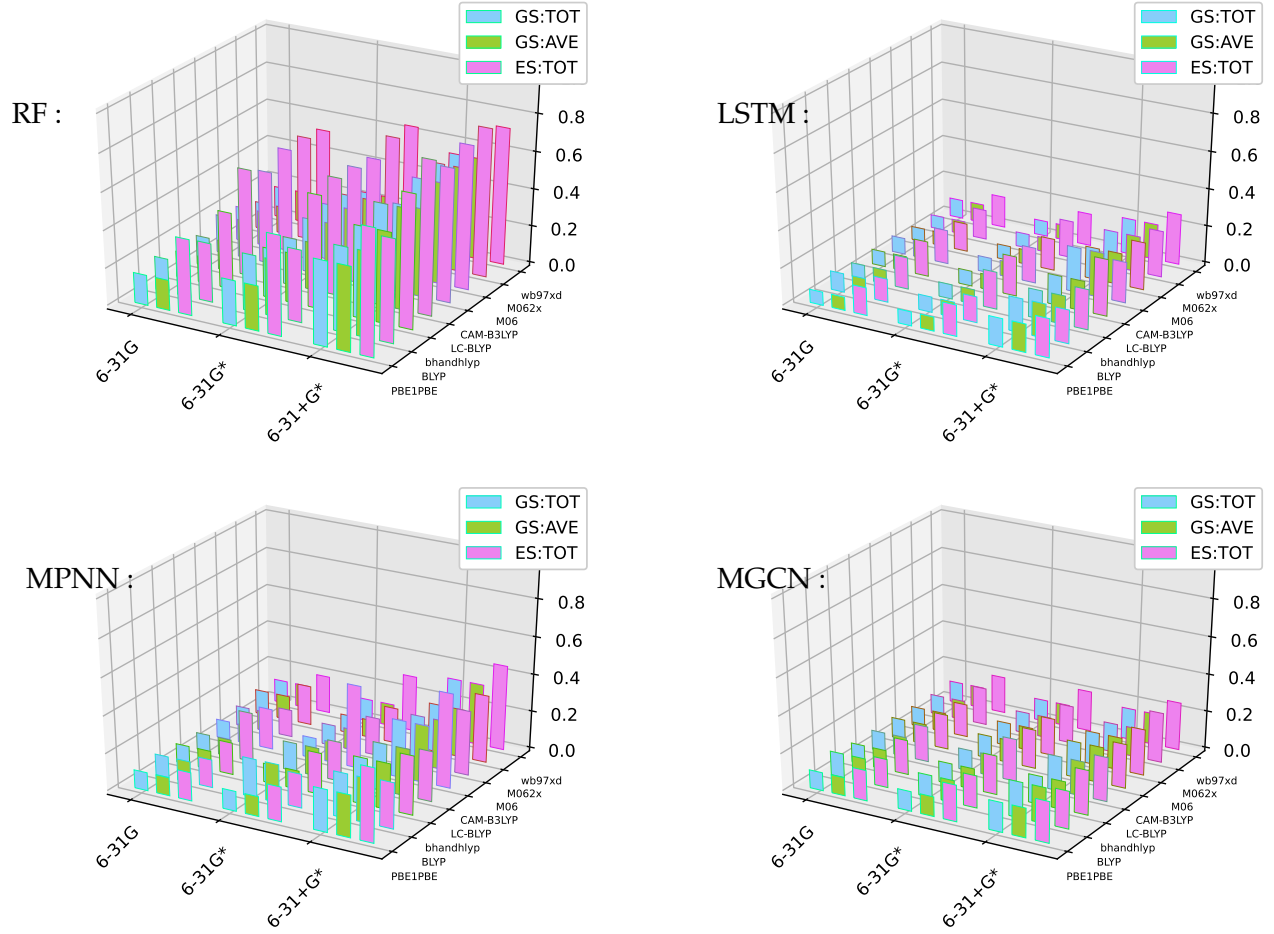


FIG. 9. MREs of the predicted total times of DFT calculations (cyan bars), predicted average times for each DFT iterations (green bars) and predicted total times of TDDFT calculations (violet bars) for the ML models.

instance, the LDA, GGA, Hybrid & Range-separated, Meta Hybrid & Range-separated Hybrid regions with magnifications of about 0.95, 1.0, 1.1, and 1.2, respectively.

For the basis sets, it can be observed in Fig.13 (top) that the computational CPU times (colored bars) matched well with the dimension of basis sets (solid line). Thus, in accordance with the change of basis sets, general polynomial curve-fitting techniques (Fig.13, bottom) can be employed to roughly consider the change of computational times.

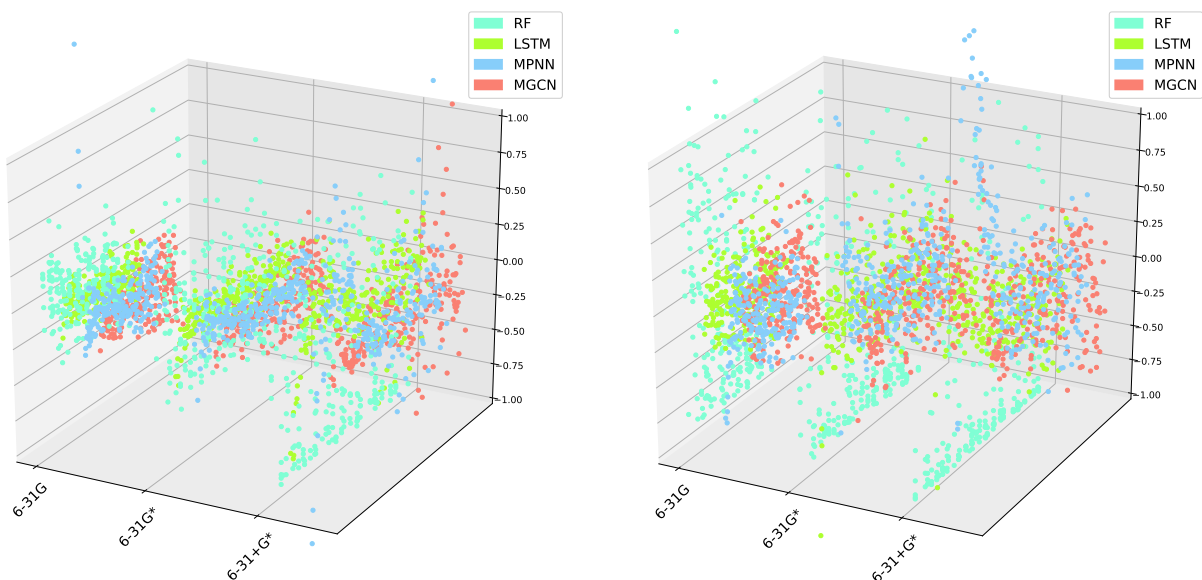


FIG. 10. The MREs of the predicted total times of DFT calculations (cyan bars), predicted average times for each DFT iterations (green bars), and the predicted total times of TDDFT calculations (violet bars) for the ML/AI models.

For the case of either-trained predictions with the trained ("trained" means the parameter was involved in pre-trained models) basis sets and untrained ("untrained" implies that the parameter was not involved in pre-trained models) DFT functionals, the trained models can be used to give the predictions with magnifications based on the types of DFT functionals. For instance, there were nine functionals together with three basis sets in Fig.9. Suppose only the models of DFT functionals of PBE and LC-BLYP were trained, then all the timing predictions for the remaining DFT functional/basis set combinations can be deduced using these existing models as the references. The obtained results were shown in Fig.14. It can be found that most derivations of predicted times were only slightly larger than the original ones except in the BLYP case, in which convergence behavior was quite different from other models. The MREs of predicted times with REF:PBE (PBE functional as the reference) and with REF:LC-BLYP (LC-BLYP functional as the reference) can still be less than 0.2 for LSTM and MPNN/MGCN models. The scatter diagrams of relative errors were also illustrated in Fig.15 for the M06-2x functional case as an instance. It can be seen that the error distributions of REF:PBE and REF:LC-BLYP cases were quite similar to the original ones for all the three basis sets. The MGCN showed

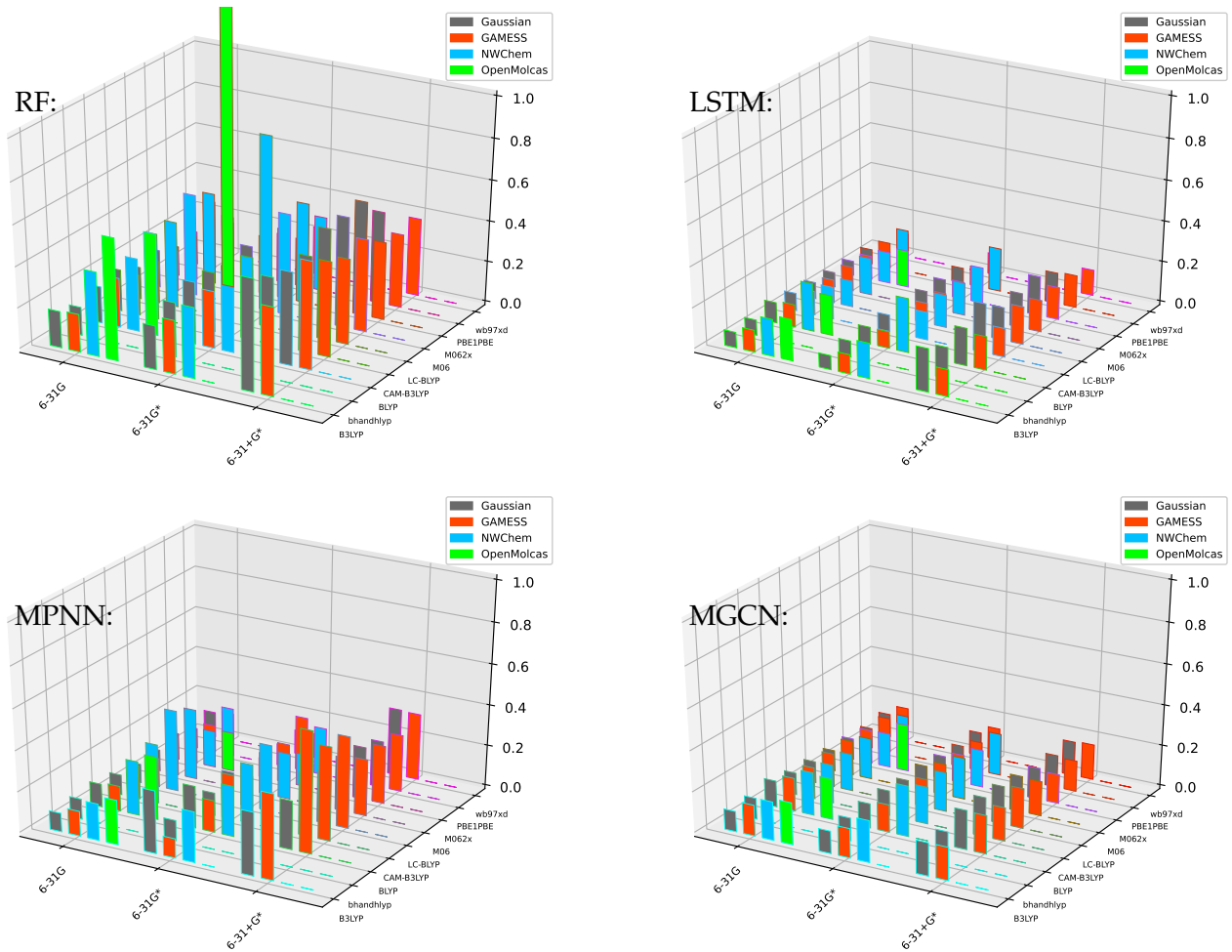


FIG. 11. Illustrations of the MREs of the predicted total times of DFT calculations using different QC packages.

the best accuracy among these three ML models with relative errors mostly distributed within +25% to -25% regions for the original case, and there were only 5% to 20% displacement for the REF:PBE and REF:LC-BLYP cases.

For the case of either-trained predictions with the trained DFT functional and untrained basis set, the pre-trained models can be used to produce predictions with magnifications based on the fitted curves from various basis sets. This procedure was similar to that of untrained DFT functionals case, while it was a bit complex as the number of basis functions has a tight relationship with the actual computational times. To obtain the magnification between reference basis sets (REF-basis) and target basis sets (TAR-basis), a three-step procedure was used : 1) choose the fitted curve of Eq.5 under the given DFT functional; 2) obtain the $f^{bas}(x_{REF})$ and $f^{bas}(x_{TAR})$ based on the fitted curve of Eq.5; 3)

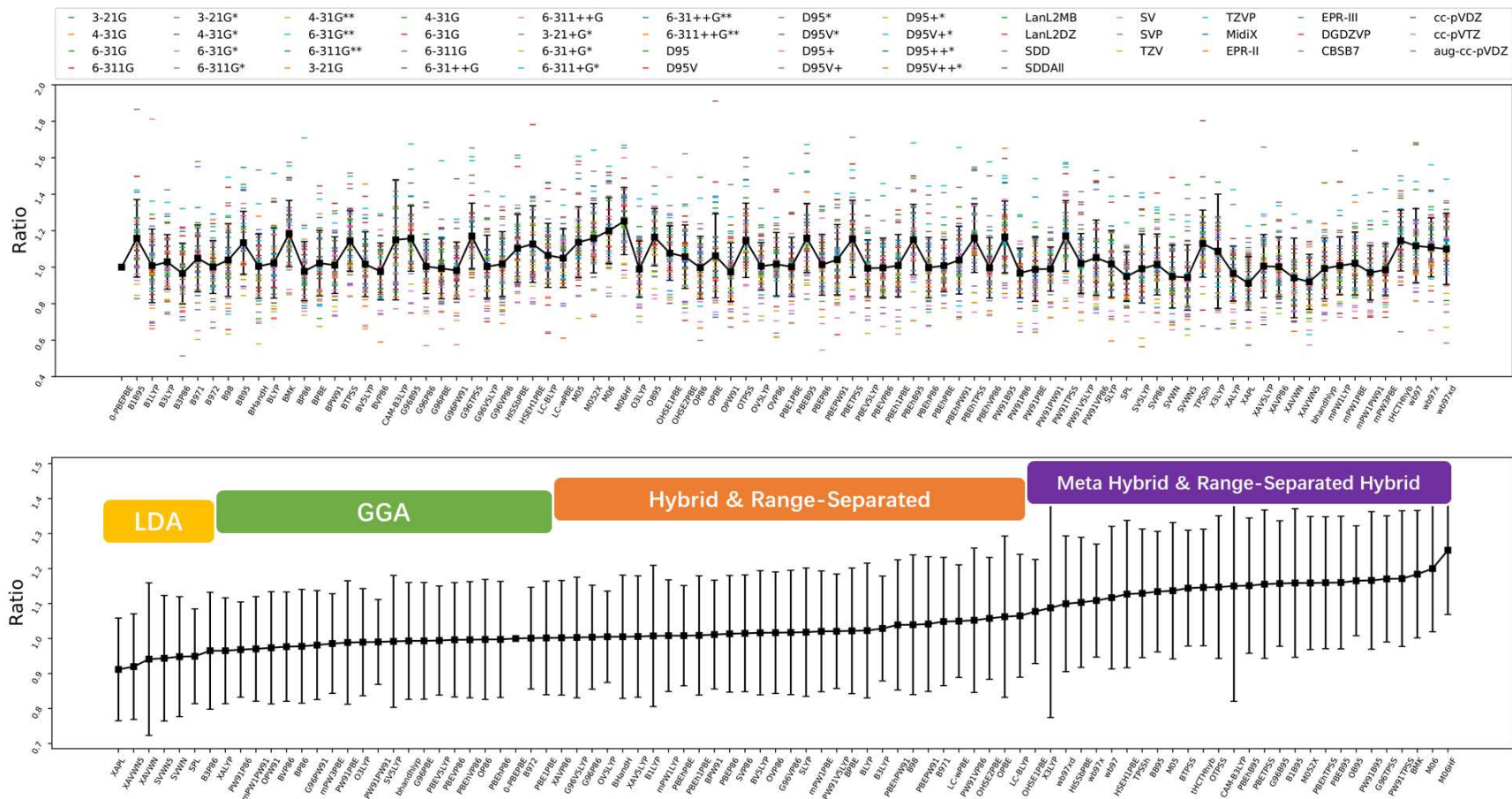


FIG. 12. **Top:** Illustrations of the ratios (colored bar) between CPU times of various DFT functionals and those of the PBE functionals for listed basis sets as shown in the legend box. **Bottom:** The ratios can be re-ordered and can be roughly partitioned for different types of DFT functionals referred to as the Jacob ladder).

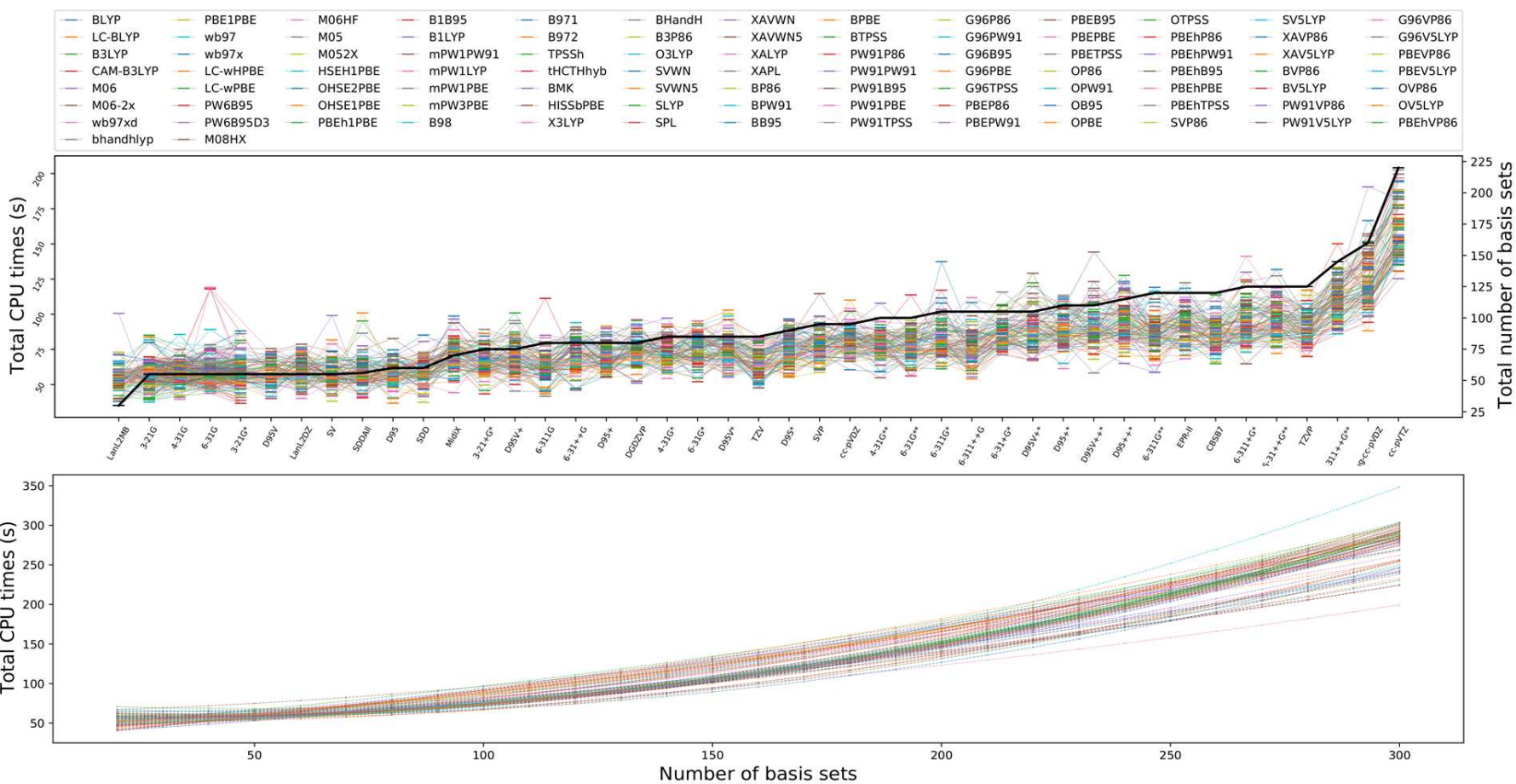


FIG. 13. **Top:** Illustrations of relationships of computational CPU times and different basis sets for listed DFT functionals and basis sets. **Bottom:** Illustrated poly-fitted curves between computational CPU times and number of basis sets for every listed DFT functionals.

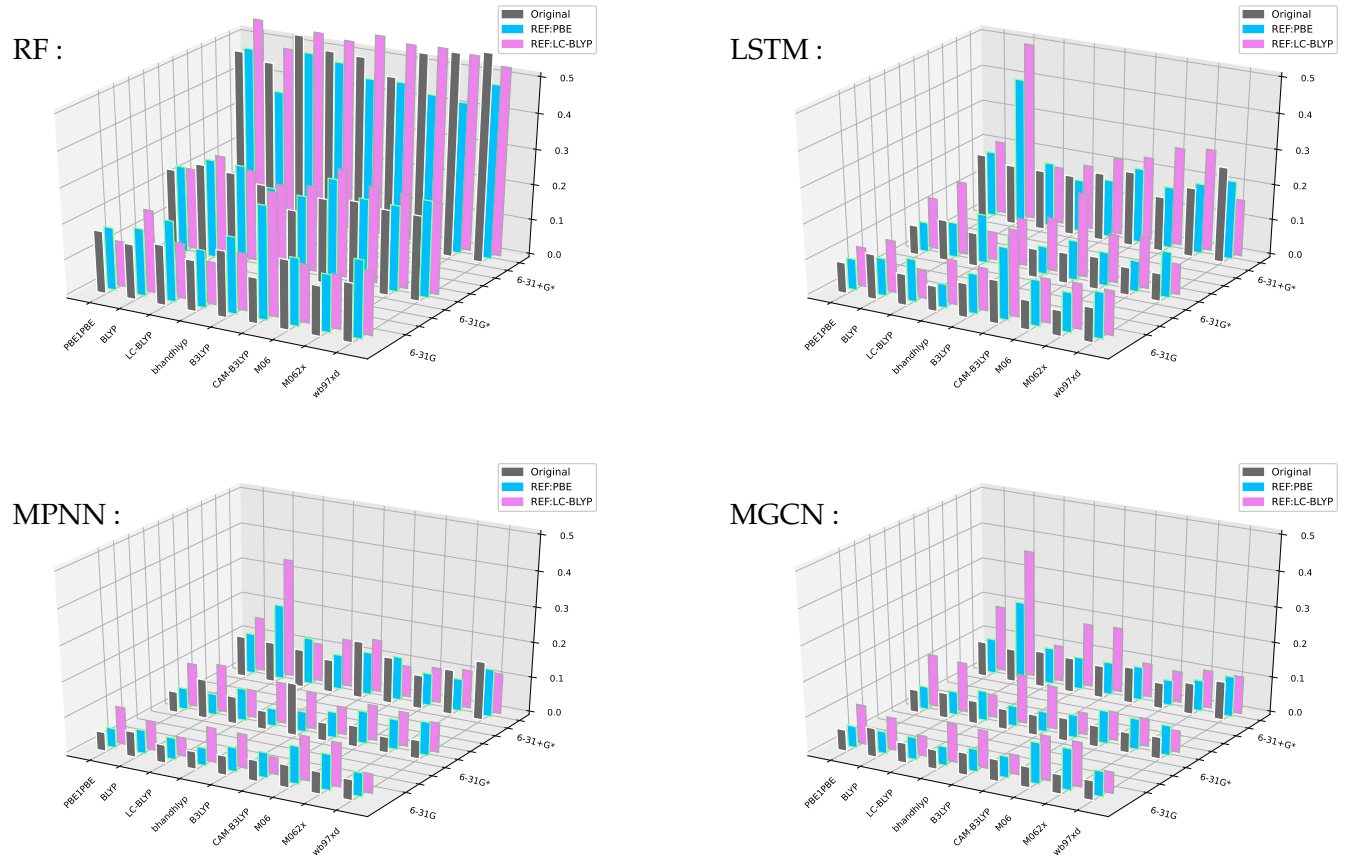


FIG. 14. Illustrations of the MRE of predicted total CPU times with trained models (original) and either-trained models (REF:PBE and REF:LC-BLYP), respectively.

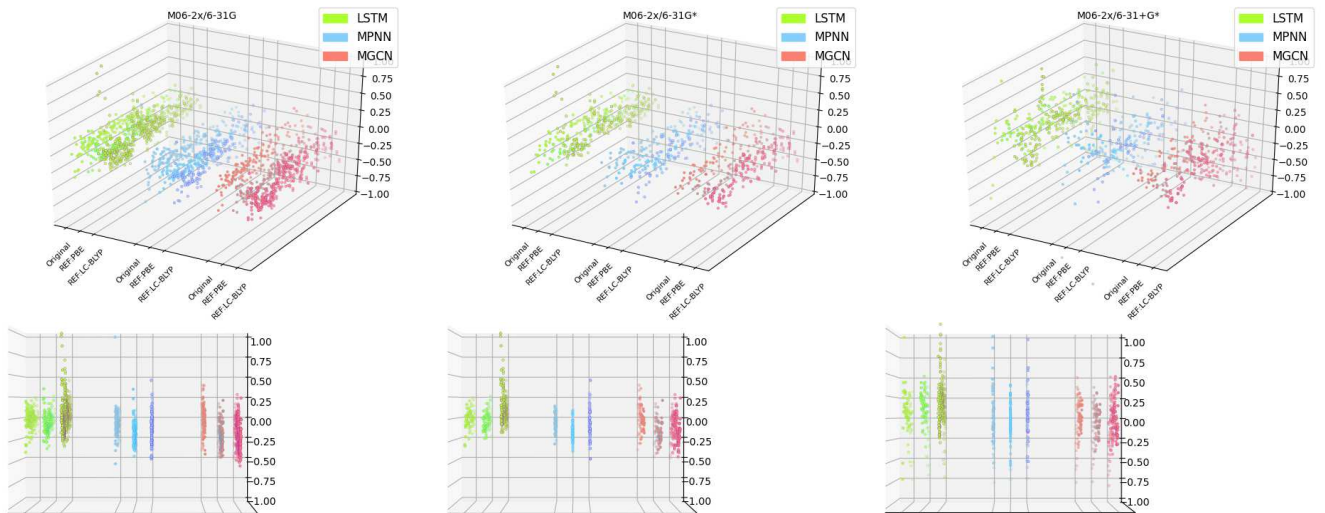


FIG. 15. Illustrations of the error scatters of predicted total CPU times using LSTM, MPNN, and MGCN models for the M06-2x cases in Fig.14. Both the stereoscopic (top) the radial (bottom) distributions are shown.

calculate the magnification coefficient c^{bas} based on Eq.4. Once the c^{bas} is obtained, the corrected timing predictions can be evaluated based on the predictions of reference basis sets. Herein, the predicted total computational CPU times for several DFT functionals together with basis sets of 6-31G, 6-31G*, 6-31+G*, 6-31++G**, SV⁹⁵, SVP⁹⁵, cc-pVDZ⁹⁶, and cc-pVTZ⁹⁶ obtained using reference basis sets of 6-31G, 6-31G*, 6-31+G* were shown in Fig.16. It can be seen that there were a lot of volatility of MREs of the original predictions that were based on the three reference basis sets (shown in the center of Fig.16). The volatility in different reference models was caused by the enlarging magnification errors when target point and the reference point in fitted curve were too far from each other. These magnification errors can be largely reduced by introducing the similarity coefficients as we explained in the previous section. The similarity-corrected results were illustrated in the outside region of Fig.16 while the error scatters were shown in Fig.17 for the sampled M06-2x cases. It can be seen that MREs can be largely reduced for all the four ML models. The graph-based MPNN and MGCN models behaved best, worse for the LSTM models, and worst for the RF models. One may notice that the relatively larger derivations for the cc-pVTZ case can be observed, it is because the 6-31G* basis set was used as the reference when applying the current similarity-corrected algorithm. The predicted timing results of cc-pVTZ basis set can be improved greatly when using 6-31+G* as the reference basis set. Additionally, one can also expect better predicted results if more basis sets can be used as the reference ones.

For the case of neither-trained predictions with the untrained DFT functional and untrained basis set, the trained models can be used to produce predictions with magnifications both from the reference DFT functional and from the reference basis set under the chemical WMI anastz. Herein, the trained models of PBE/6-31G, PBE/6-31G*, and 6-31+G* combinations were used as the references, and total CPU times were predicted using the neither-trained models for several different combinations of DFT functionals and basis sets. The calculated MREs of predicted total CPU times were illustrated in Fig.18 and the error scatters were shown in Fig.19. It can be noticed that the illustrated results were quite similar with those in Fig.16. The graph-based MPNN and MGCN models still exhibited best, worse for the LSTM models, and worst behaviours for the RF models. Additionally, the reference basis set again played important role in the predicted results.

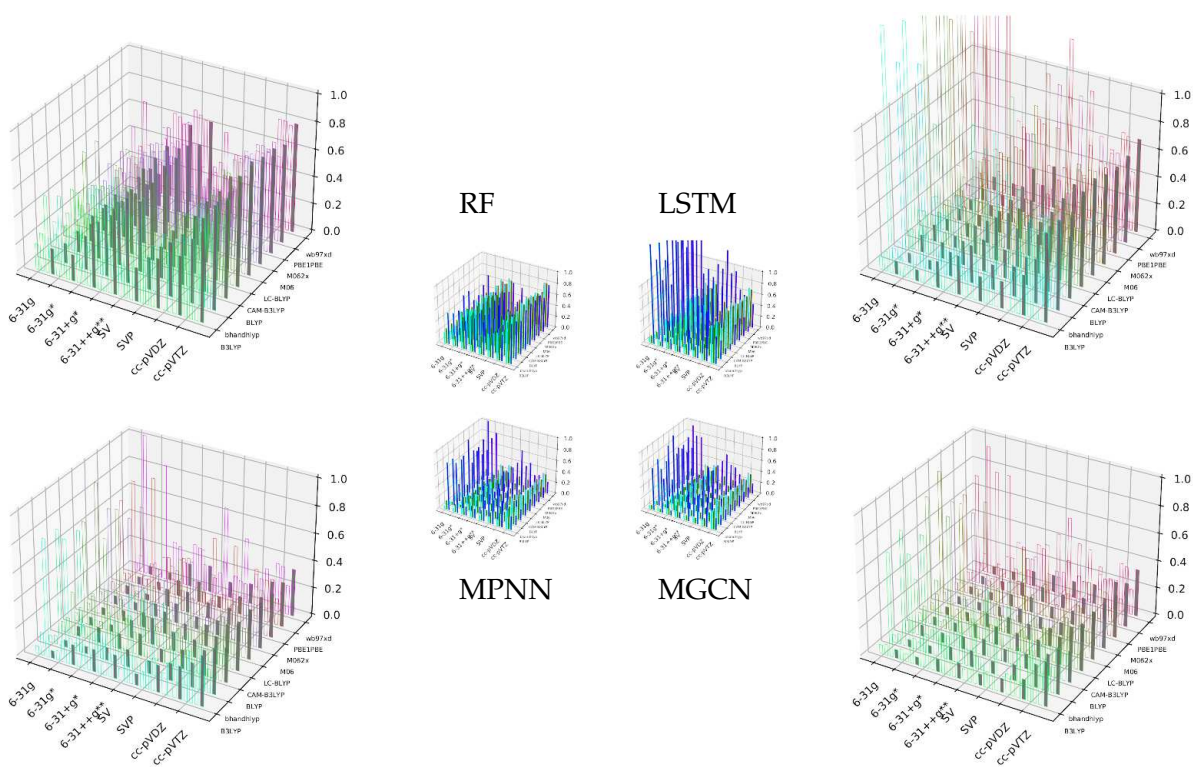


FIG. 16. Illustrations of the MREs of predicted total CPU times using RF, LSTM, MPNN and MGCN models with 6-31G, 6-31G*, 6-31+G* reference basis sets (center), and the similarity-corrected ones for practical predictions (outside).

V. CONCLUSION

A forecasting system for computational time of DFT/TDDFT calculations is presented in this work. Four popular ML methods, including the RF, LSTM, MPNN, and MGCN models, were used to produce reliable predicted timing results for DFT/TDDFT calculations. The structural similarity (in RF), recognition of chemical formula (in LSTM), and spatial structures (in MPNN and MGCN) were the ideas behind the choice of working ML models. The cheminformatics with SMILES codes and graph-based spatial structures were employed for extracting structural information when training and testing the ML models. The use of cheminformatics also reduced the number of training suits significantly compared to that of the case when performing image recognition tasks. Moreover, various combinations of DFT functional and basis set can be demonstrated by employing the proposed chemical MWI ansatz using either-trained or neither-trained models.

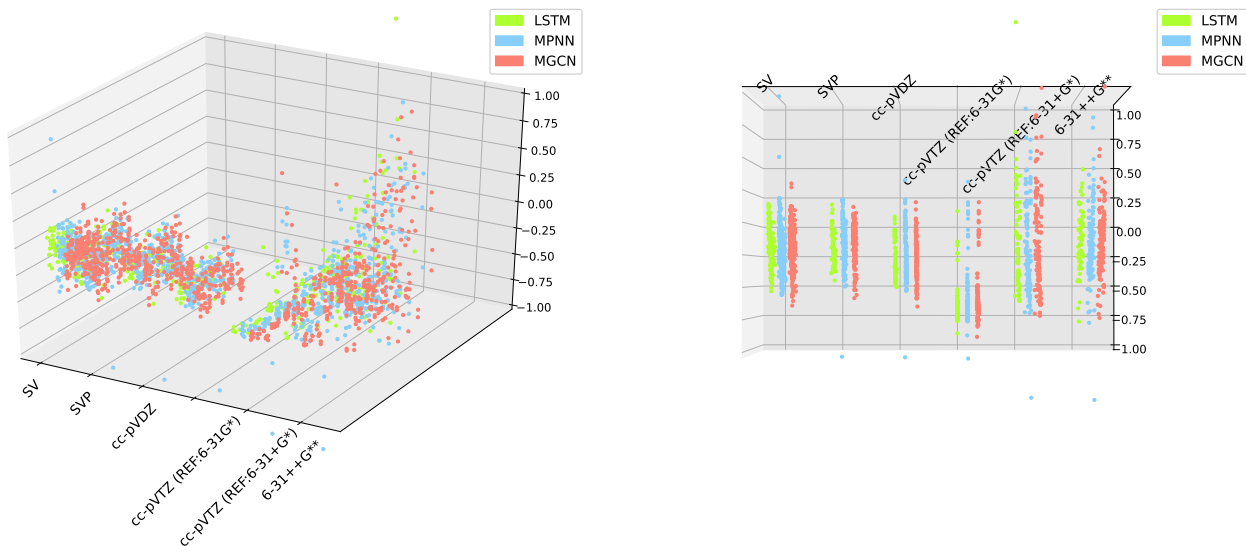


FIG. 17. Illustrations of the error scatters of predicted total CPU times using LSTM, MPNN, and MGCN models for the M06-2x cases in Fig.16. Both the stereoscopic (left) the radial (right) distributions are shown.

The four ML models can be used as the kernels for running the forecasting system. The overall performance followed the "LSTM \rightarrow MGCN \rightarrow MPNN \rightarrow RF" order in the chemical space with the pre-trained ML models, and the typical MREs were 0.1 to 0.2 for the first two (LSTM/MGCN) models with +25% to -25% relative errors for most molecules. The tendency order in performance turned to "MGCN \sim MPNN \rightarrow LSTM \rightarrow RF" in the chemical space without the pre-trained ML models and the typical MREs were still within the scope of 0.1 to 0.2 for the first two (MGCN/MPNN) models irrespective of whether either-trained or neither-trained cases was used. The distribution of relative errors was only slightly enlarged. The relatively small MREs and concentrated relative errors showed that the forecasting system can be used in the HPC's task assignment and load-balancing applications. We are currently working in this direction, particularly in coordination with fragmentation approaches in quantum chemistry, such as molecular fractionation with conjugate caps⁹⁷⁻⁹⁹ and the renormalized exciton method¹⁰⁰⁻¹⁰².

At this stage, mainly the CPU wall time predictions on solving the Kohn-Sham equations as well as their TD expansions in single-point calculations are presented. This type of calculation is representative for the computational cost of a molecule⁸, thus it is used

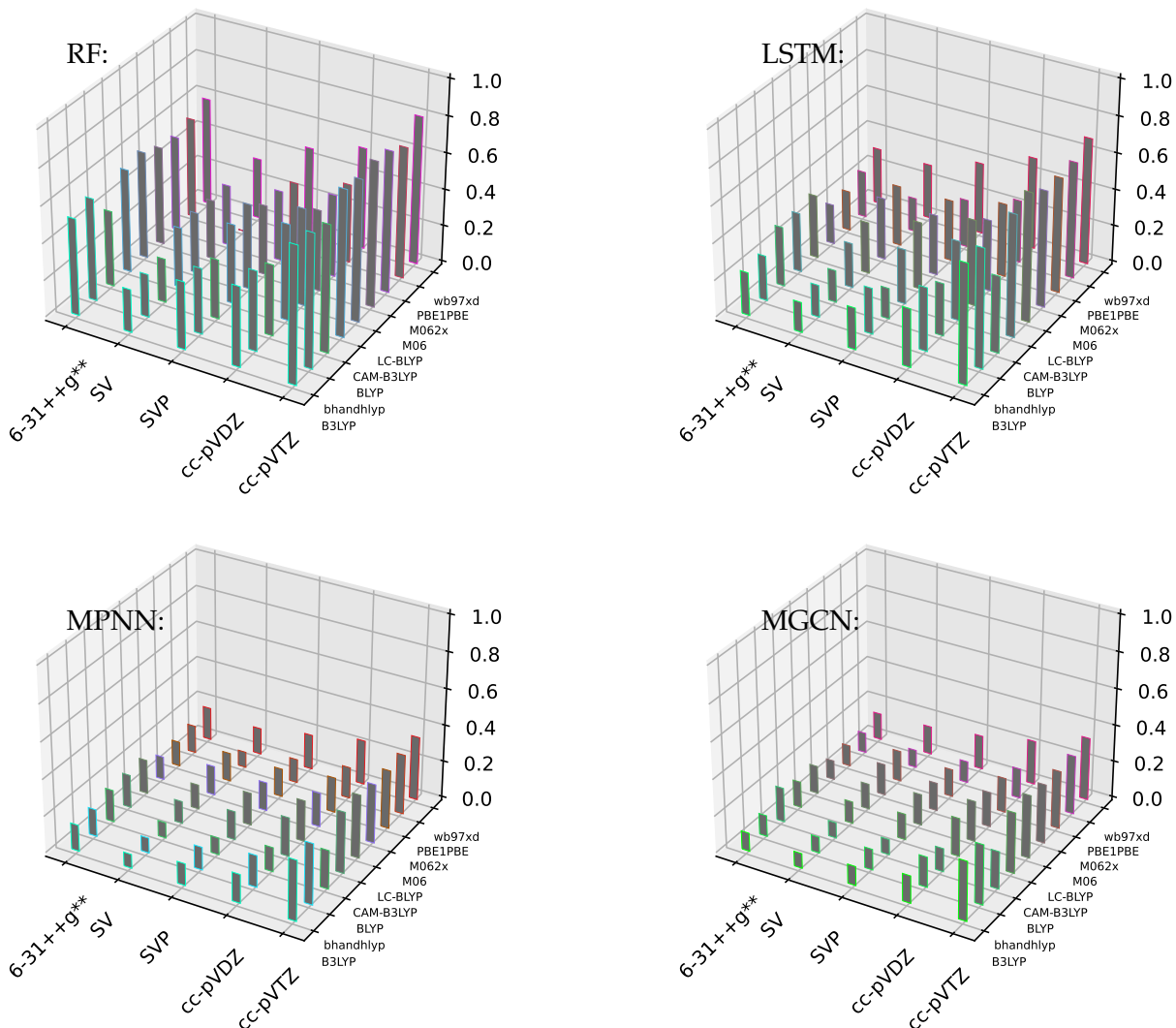


FIG. 18. Illustrations of the MREs of predicted total CPU times with neither-trained models.

as the first step in the design of a forecasting system. The routine calculations such as geometry-optimization, frequencies calculations are not yet included in these predictions, and are on the list of our future works.

VI. ACKNOWLEDGEMENT

The work was supported by the National Key Research and Development Program of China (Grant No.2018YFB0203805), National Natural Science Foundation of China (Grant No.21703260), the Informationization Program of the Chinese Academy of Science (Grant No.XXH13506-403), and the Guangdong Provincial Key Laboratory of Bio-computing (Grant No.2016B030301007). We also thank PARATERA company for their

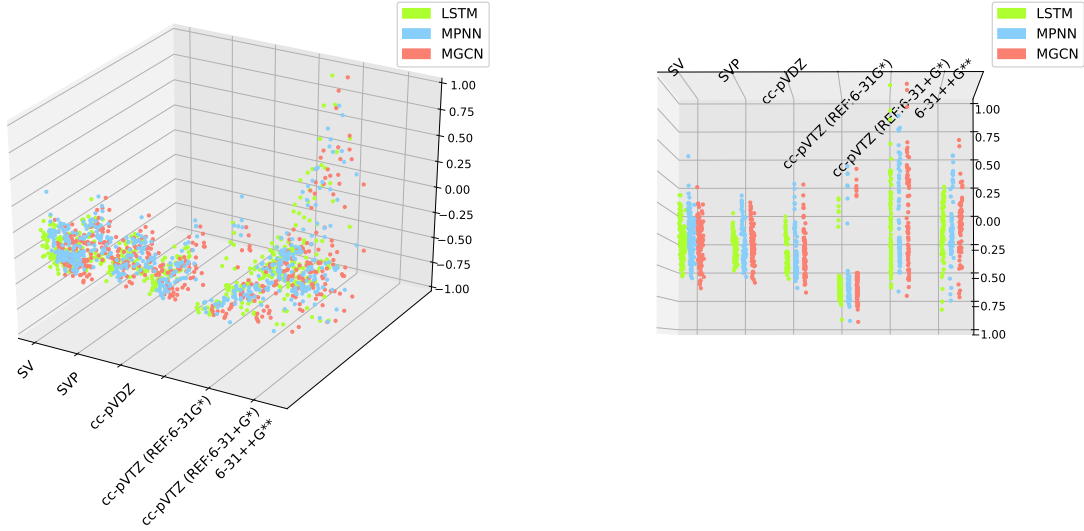


FIG. 19. Illustrations of the error scatters of predicted total CPU times using LSTM, MPNN, and MGCN models (neither-trained) for the M06-2x cases in Figure.18.

cooperation.

VII. APPENDIX

A. Kohn-Sham density functional theory and its scaling

In the Born-Oppenheimer approximation, a stationary electronic state can be described by a wave function $\Psi(\vec{r}_1, \dots, \vec{r}_N)$ satisfying the many-electron time-independent Schrödinger equation,

$$\hat{H}\Psi = [\hat{T} + \hat{V} + \hat{U}] \Psi = \left[\sum_{i=1}^N \left(-\frac{\hbar}{2m_i} \nabla_i^2 \right) + \sum_{i=1}^N V(\vec{r}_i) + \sum_{i<j}^N U(\vec{r}_i, \vec{r}_j) \right] \Psi = E\Psi, \quad (\text{A.1})$$

where \hat{H} denotes the electronic Hamiltonian, E denotes the total energy, \hat{T} denotes the kinetic energy, \hat{V} denotes the potential energy from an external field due to positively charged nuclei, and \hat{U} denotes the electron-electron interaction energy.

In the KS-DFT hypothesis, particles can be treated as non-interacting fermions, so that there exists an orthogonal and normalized function set $\{\phi_i^{\text{KS}} | i = 1, 2, \dots, N\}$ satisfying the condition:

$$\rho(\vec{r}) = \rho_s(\vec{r}) = \sum_{i=1}^N |\phi_i^{\text{KS}}(\vec{r})|^2 \quad (\text{A.2})$$

Here, $\rho(\vec{r})$ denotes the probability density of ground state electrons in a factual system and $\rho_s(\vec{r})$ denotes a fictitious system. Thus, the KS wave function is a single Slater determinant constructed from a set of function sets (i.e., orbitals) that are the lowest energy solutions to

$$\left[-\frac{\hbar}{2m_1}\nabla_1^2 - \sum_A \frac{Z_A}{r_{1A}} + \int \frac{\rho(\vec{r}_2)}{r_{12}} d\vec{r}_2 + V_{XC}(1)\right]\phi_i^{KS}(1) = \varepsilon_i^{KS}\phi_i^{KS}(1), \quad (\text{A.3})$$

where the $V_{XC}(1)$ is referred to as exchange-correlation potential, and the "(1)" following each operator symbol simply indicates that the operator is 1-electron in nature. This equation is very similar to the Fock equation,

$$\left[-\frac{\hbar}{2m_1}\nabla_1^2 - \sum_A \frac{Z_A}{r_{1A}} - \frac{1}{2} \int \int \frac{\rho(\vec{r}_1)\rho(\vec{r}_2)}{r_{12}} d\vec{r}_1 d\vec{r}_2\right]\phi_i^{HF}(1) = \varepsilon_i^{HF}\phi_i^{HF}(1), \quad (\text{A.4})$$

that is used in HF theory. Both Eq.(A.3) and Eq.(A.4) can be solved iteratively using the so-called self-consistent field (SCF) methods. During the SCF iteration, orbital ϕ_i is updated iteratively, and is used to calculate electron density ,

$$\rho(\vec{r}) = \sum_{i=1}^N |\phi_i(\vec{r})|^2, \quad (\text{A.5})$$

which in turn, determines the one-electron matrix (e.g., Fock matrix in SCF iterations) to be diagonalized. After several iterations, both molecular orbital ϕ_i and its energy ε_i can be obtained, and the total electronic energy can then be calculated.

Comparing Eq.(A.3) with Eq.(A.4), one can clearly see that the major difference between them is in the two-electron integrals component. The origin of the N^4 scaling behavior is the calculation of four-center two-electron integrals, i.e.,

$$(\mu\nu|\lambda\sigma) = \int \int \phi_\mu(1)\phi_\nu(1)\frac{1}{r_{12}}\phi_\lambda(2)\phi_\sigma(2)d\tau_1d\tau_2, \quad (\text{A.6})$$

where μ, ν, λ , and σ denote indices of atomic orbitals. This scaling is also the upper boundary for the HF or hybrid DFT calculations. However, many two-electron integrals are of negligible magnitude for large molecules, and some rigorous upper boundary conditions can be applied to the integrals. For instance, the Schwarz inequality⁴⁰

$$|(\mu\nu|\lambda\sigma)| \leq \sqrt{(\mu\nu|\mu\nu)(\lambda\sigma|\lambda\sigma)} \quad (\text{A.7})$$

allows the calculation of strict, mathematical upper bounds of all two-electron integrals to be computed in an $N^2 \log N$ process. Apart from the calculation of the two-electron

integrals, the diagonalization of the Fock or Fock-like matrix is expected to contribute significantly to the computational cost because the diagonalization step scales intrinsically as N^3 ; or even lower if the matrix (e.g., in large enough molecule) to be diagonalized is sufficiently sparse.

Nevertheless, it can be noticed that for the hybrid DFT functionals, a hybrid exchange-correlation functional (i.e., the $V_{XC}(1)$ term in Eq.(A.3)) is usually constructed as a linear combination of the third terms (HF exact exchange functional) in Eq.(A.4). Hence, hybrid DFT methods scale in a similar manner to the HF but are normally more expensive due to a larger proportionality term, involved while the pure DFT methods scale better than HF because there is no HF exchange.

B. ML models used in the forecasting system

1. RF model together with simple feed-forward neural networks

We used the feed-forward neural network (FNN) as the skeletal frame to obtain the model between basis number and the computational time. FIG.A.1 shows an illustration of the FNN model. Four layers are used in our model, which are input layer, two hidden layers, and the output layer. The "input layer" is constructed using the system magnitude features (e.g., number of basis sets) and the computational time. These vectors are normalized and then fed to the hidden layers. Each "hidden layer" contains several neurons, and the TANH function is used as the activation function. The data passed from the hidden layer will be directly used in the linear combination of the output results.

The predicted result for a molecule that is far from the training set and will still be very poor, if we only use the FNN model of FIG.A.1, To overcome the dependency of training sets, we introduced the idea of "feature training". "Feature training" means that few molecules suites with specific features (e.g. linear(L), dendritic(D), ring(R), etc.) will be trained as the "cost functions", upon which the computational cost (y) for any molecule can be calculated by a linear combination of these "cost basis", e.g.,

$$y = p_L \cdot f_L(x) + p_D \cdot f_D(x) + p_R \cdot f_R(x) + \dots, \quad (\text{A.8})$$

where p_L , p_D and p_R denote the possibilities for each "cost basis" $f_{feature}(x)$, the $f_{feature}$ denotes the "cost functions", and the $f_{feature}(x)$ denotes the expected computational cost

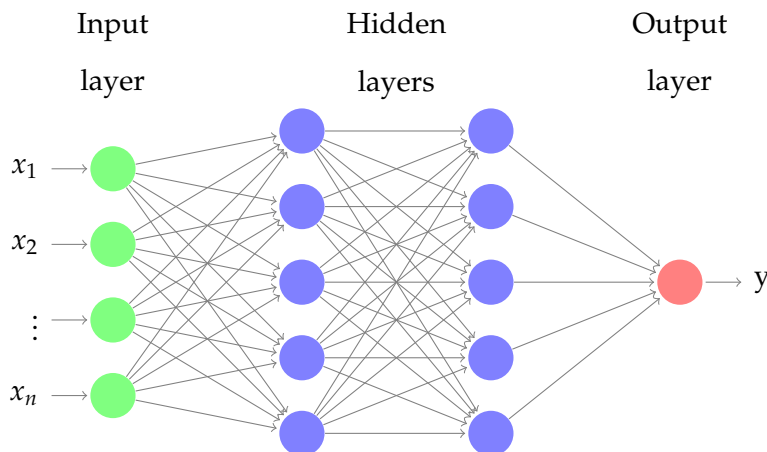


FIG. A.1. The simple FNN model.

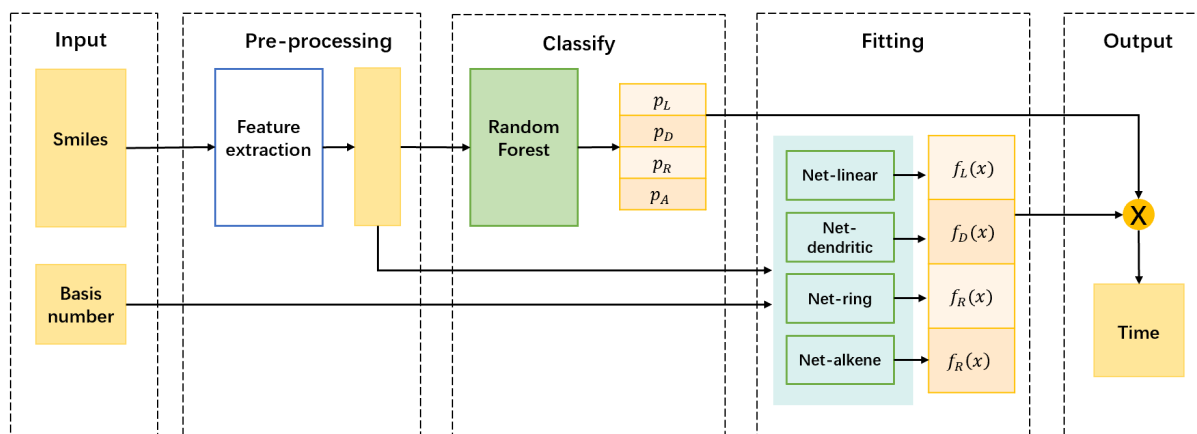


FIG. A.2. Architecture of RF with FNNs.

for the "feature" model with magnitude parameter x . Herein, one can notice that this "feature training" ansatz matches well with the RF model used in ML/AI. Under this ansatz, a specific model (i.e. cost function) is trained and saved for each structure of the molecular suit. Afterwards, an RF classifier is used to place the molecules into given categories, such as linear, dendritic or ring molecules, etc., with possibilities (p). The classifier accepts the SMILES codes of molecules as its input. The number of every molecule's atoms (with hydrogen atoms excluded), branches, atoms on branches and cycles is calculated and combined as an input vector according to its SMILES code. Fig.A.2 illustrates entire process.

In training :

The coefficients for each "cost basis" were obtained via the RF classifier with the SCIKIT-LEARN(SKLEARN)¹⁰³ package, with all the parameters set to default values. The classifier provides a molecule's probability of falling into each category as the output, which can be used in Eq.(A.8) for the predictions.

2. *Bi-LSTM with attention*

The kinds of features extracted by the RF classifier are designed artificially with subjective preference, so that it may be not enough for aggregating molecular structural information. Considering that we used textual data (i.e., SMILES code) as the representation of molecular structure, methods for natural language processing (NLP) are thus, suitable for feature extraction as a result of this issue.

Here, we use the bidirectional LSTM(Bi-LSTM) with attention model that was proposed by Peng and his coworkers.¹⁰⁴ It is the state-of-the-art model for relation classification tasks; thus, we used this model to extract structural features from SMILES. Fig.A.3 illustrates the architecture of the model. The input features include the SMILES code (in the form of one-hot) and the number of basis functions. Suppose every character in a T-length SMILES sequence is denoted with a one-hot vector x_i , x_i will be converted to a real number vector e_i ($e_i = Wx_i$, where W denotes a parameter matrix automatically learned by the model during training). Then $E = \{e_1, e_2, \dots, e_t\}$ is sent to the Bi-LSTM layer. The Bi-LSTM layer consists of a forward layer and a backward layer so that the model can learn from forward and backward sequences as the past and future semantic information in a sentence are equivalently significant. The LSTM layers at two directions generate two outputs, H_f and H_b :

$$H_f = L(E), \quad H_b = L(E), \quad (\text{A.9})$$

where L denotes the operations performed by a LSTM layer. Then an attention layer accepts the sum of the outputs from Bi-LSTM layers:

$$H = H_f + H_b. \quad (\text{A.10})$$

The attention mechanism allows different context vectors to be generated from the Bi-LSTM layer's output at every time step by assigning different "attention weight" to

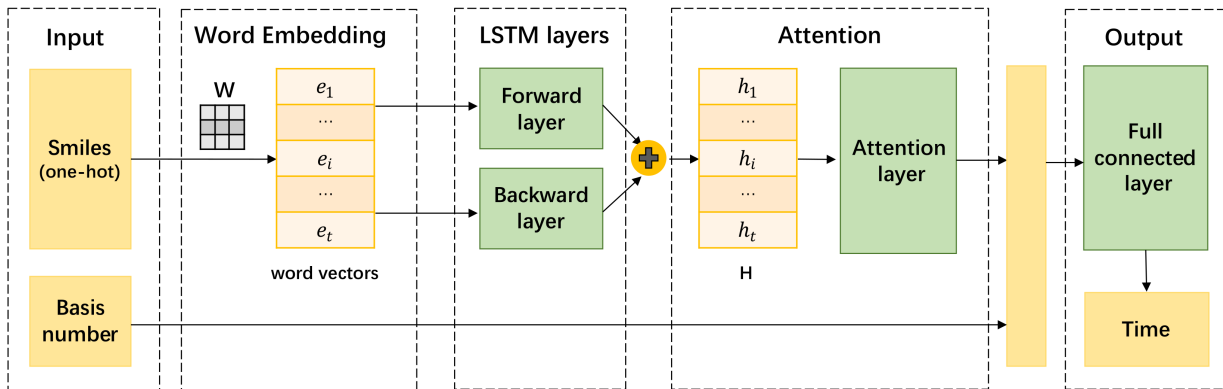


FIG. A.3. Architecture of Bi-LSTM with attention model.

the outputs. Without the attention mechanism, the feature extraction operation on the output at every time step would have the limitation of depending on one same context vector with fixed length invariant to time steps. The attention layer outputs the final representation c of a SMILES as

$$\alpha = softmax(w^T tanh(H)), \quad (A.11)$$

$$c = H\alpha^T, \quad (A.12)$$

where α denotes the attention weight vector, and w denotes a trained parameter vector. The high-level features of molecular structures are produced after the attention layer. We combine the structural features and the number of basis functions and feed them into fully-connected layers to get the predicted result.

3. MPNN model

As a representation of molecular structure, SMILES is quite inexact due to absence of spatial information. Fig.A.4 shows that for a more accurate representation, it is rational to model a molecule using an undirected graph G . We use the MPNN model, which is recognized as a kind of graph neural network (GNN) proposed by Gilmer as a solution for graph-based learning.⁵⁸

The initial inputs of the model include a feature vector collection for nodes of the graph, denoted with x_v , containing features of atom types, aromaticity and hybridization types, and a feature vector collection for edges, denoted with e_{vw} , containing features of bond types. Further, the model has two phases: a message passing phase and a readout

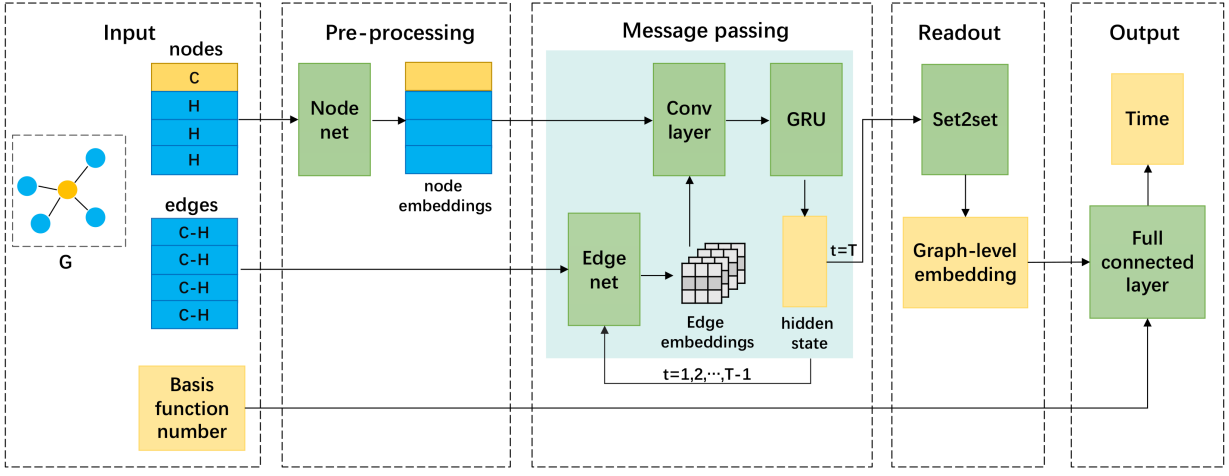


FIG. A.4. Architecture of the MPNN model.

phase. The message passing phase runs T -step graph convolutions and at each step t , it is defined in terms of a message function M_t and a vertex update function U_t . Before the message passing, the node vectors are mapped to a $n \times d$ matrix called "node embedding" by a network (called "node net"), with n denoting the number of nodes; and d representing the dimension of hidden state of each node. During the message passing phase, hidden states h_v^t of each node are updated according to messages m_v^{t+1} . The message passing phase can be summarized as

$$m_v^{t+1} = \sum_{w \in N(v)} M_t(h_v^t, h_w^t, e_{vw}), \quad (\text{A.13})$$

$$h_v^{t+1} = U_t(h_v^t, m_v^{t+1}), \quad (\text{A.14})$$

where $N(v)$ denotes the neighbours of v in G . M_t is defined as $M(h_v, h_w, e_{vw}) = A(e_{vw})h_w$ specifically, where $A(e_{vw})$ denotes a network (edge net) mapping each edge vector e_{vw} to a $d \times d$ matrix (edge embedding). The vertex update function is GRU, short for gated recurrent unit.¹⁰⁵ At the readout phase, a feature vector can be obtained as a summary of the whole graph with a readout function R

$$\hat{y} = R(\{h_v^T | v \in G\}), \quad (\text{A.15})$$

where R denotes the *set2set*¹⁰⁶ model. The *set2set* model produces a graph-level embedding that is invariant to the order of nodes. Finally, we combine the graph-level embedding and the basis function number and feed them to fully-connected networks to get the prediction results. Fig.A.4 illustrates the architecture of the MPNN model.

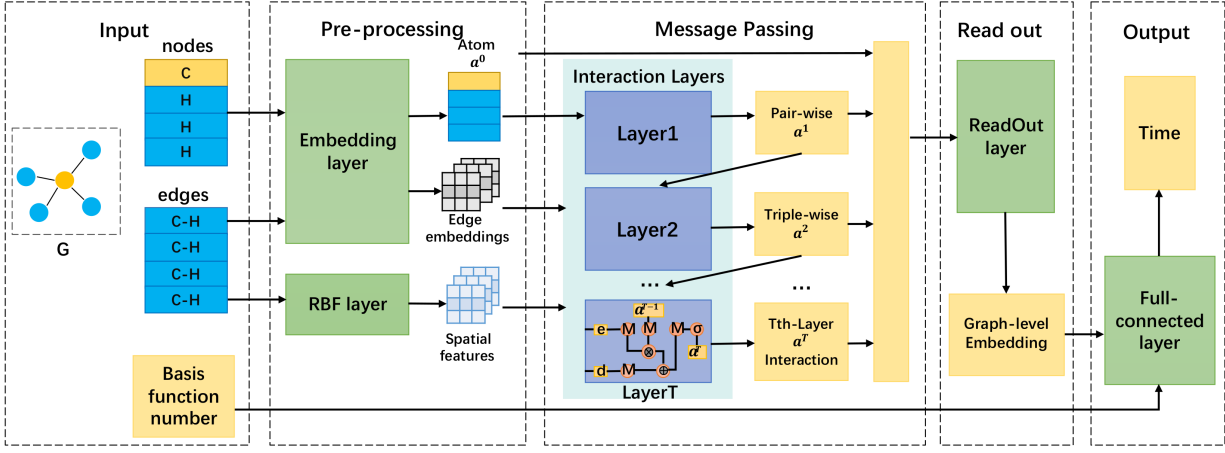


FIG. A.5. Architecture of the MGCN model.

4. MGCN model

Apart from MPNN, we also introduced another GNN model, MGCN⁵⁹, which is reported to have the advantages of generalizability and transferability. As shown in Fig.A.5, the architecture of MGCN includes five phases. First, the initial inputs of the model include a feature vector collection for nodes of the graph, denoted by $a^0 \in \mathbb{R}^D$, containing features of atom types, aromaticity and hybridization types, a feature vector collection for edges, denoted by $e \in \mathbb{R}$, containing features of bond types and bond lengths, and the number of the basis functions. At the pre-processing phase, the embedding layer generates the node atom embeddings ($A^0 \in \mathbb{R}^{N \times D}$) and edge embeddings ($E \in \mathbb{R}^{N \times N \times D}$). The radial basis function (RBF)^{107,108} layer converts the bond lengths to a distance tensor $D \in \mathbb{R}^{N \times N \times K}$, with d_{ij} representing the distance between atom i and atom j . The RBF layer's function form can be expressed as

$$RBF(x) = \sum_{i=1}^K h(||x - \mu_i||), \quad (\text{A.16})$$

where \cup denotes concatenation and μ_i is from a set of K central points $\{\mu_1, \dots, \mu_K\}$. At the message passing phase, the interaction layers are constructed in the form of hierarchical architecture to simulate the quantum interactions which are transformed at different levels (atom-wise, atom-pair, atom-triple, etc.). The l -th layer generates an edge presentation e_{ij}^{l+1} and an atom representation a_i^{l+1} :

$$e_{ij}^{l+1} = h_e(a_i^l, a_j^l, e_{ij}^l), \quad (\text{A.17})$$

$$a_i^{l+1} = \sum_{j=1, j \neq i}^N = h_v(a_j^l, e_{ij}^l, d_{ij}), \quad (\text{A.18})$$

where h_e denotes the edge update function and h_v denotes the message passing function, respectively. The form of h_e is as follows:

$$h_e = \eta e_{ij}^l \oplus (1 - \eta) W^{ue} a_i^l \odot a_j^l. \quad (\text{A.19})$$

Here η denotes a constant set to 0.8, W^{ue} denotes a weight matrix, \oplus denotes elementwise addition and \odot is the elementwise dot product. The form of h_v is

$$h_v = \tanh(W^{uv} (M^{fa}(a_j^l) \odot M^{fd}(d_{ij}) \oplus M^{fe}(e_{ij}))), \quad (\text{A.20})$$

where $M(x)$ denotes a linear layer which is in the form $M(x) = Wx + b$. The outputs of T interaction layers along with a_i^0 are concatenated together as

$$a_i = \bigcup_{k=0}^T a_i^k. \quad (\text{A.21})$$

Afterwards, The Readout layer generates a graph-level embedding G as

$$G = \sum_{i=1}^N W^{r2} \sigma(M^{r1}(a_i)) + \sum_{i=1}^N \sum_{j=1, j \neq i}^N W^{r2} \sigma(M^{r1}(e_{ij})). \quad (\text{A.22})$$

Here σ denotes the softplus function. Finally, G and the basis function number are concatenated and sent to a fully-connected layer to get the prediction time.

REFERENCES

- ¹Friesner, R. A. Ab initio quantum chemistry: Methodology and applications. *Proc. Natl. Acad. Sci. U.S.A* **2005**, *102*, 6648–6653.
- ²Hergert, H.; Bogner, S.; Morris, T.; Schwenk, A.; Tsukiyama, K. The In-Medium Similarity Renormalization Group: A novel ab initio method for nuclei. *Phys. Rep.* **2016**, *621*, 165 – 222, Memorial Volume in Honor of Gerald E. Brown.
- ³Al-Douri, Y.; Hashim, U.; Khenata, R.; Reshak, A.; Ameri, M.; Bouhemadou, A.; Ruslinda, A. R.; Arshad, M. M. Ab initio method of optical investigations of CdS1-xTex alloys under quantum dots diameter effect. *Sol. Energy* **2015**, *115*, 33 – 39.
- ⁴Scerri, E. R. Has chemistry been at least approximately reduced to quantum mechanics? PSA: Proceedings of the biennial meeting of the philosophy of science association. 1994; pp 160–170.

- ⁵Bash, P. A.; Ho, L. L.; MacKerell, A. D.; Levine, D.; Hallstrom, P. Progress toward chemical accuracy in the computer simulation of condensed phase reactions. *Proc. Natl. Acad. Sci. U.S.A* **1996**, *93*, 3698–3703.
- ⁶Zhao, L.; Pan, S.; Holzmann, N.; Schwerdtfeger, P.; Frenking, G. Chemical bonding and bonding models of main-group compounds. *Chem. Rev.* **2019**, *119*, 8781–8845.
- ⁷Jensen, F. *Introduction to computational chemistry*; John Wiley & sons, 2017; pp 80–81.
- ⁸Helgaker, T.; Jorgensen, P.; Olsen, J. *Molecular electronic-structure theory*; John Wiley & Sons, 2014; pp 142–200.
- ⁹Møller, C.; Plesset, M. S. Note on an Approximation Treatment for Many-Electron Systems. *Phys. Rev.* **1934**, *46*, 618–622.
- ¹⁰Purvis, G. D.; Bartlett, R. J. A full coupled-cluster singles and doubles model: The inclusion of disconnected triples. *J. Chem. Phys.* **1982**, *76*, 1910–1918.
- ¹¹Cullen, J. M.; Zerner, M. C. The linked singles and doubles model: An approximate theory of electron correlation based on the coupled-cluster ansatz. *J. Chem. Phys.* **1982**, *77*, 4088–4109.
- ¹²Szalay, P. G.; Müller, T.; Gidofalvi, G.; Lischka, H.; Shepard, R. Multiconfiguration Self-Consistent Field and Multireference Configuration Interaction Methods and Applications. *Chem. Rev.* **2012**, *112*, 108 – 181.
- ¹³Brock, D. C.; Moore, G. E. *Understanding Moore’s law: four decades of innovation*; Chemical Heritage Foundation, 2006.
- ¹⁴Heinen, S.; Schwilk, M.; von Rudorff, G. F.; von Lilienfeld, O. A. Machine learning the computational cost of quantum chemistry. *Mach. Learn.: Sci. Technol.* **2020**, *1*, 025002.
- ¹⁵Downey, A. Predicting queue times on space-sharing parallel computers. Proceedings 11th International Parallel Processing Symposium. Genva, Switzerland, 1997; pp 209–218.
- ¹⁶Smith, W.; Taylor, V.; Foster, I. In *Job Scheduling Strategies for Parallel Processing*; Goos, G., Hartmanis, J., van Leeuwen, J., Feitelson, D. G., Rudolph, L., Eds.; Springer Berlin Heidelberg: Berlin, Heidelberg, 1999; Vol. 1659; pp 202–219, Series Title: Lecture Notes in Comput. Sci.
- ¹⁷Tsafrir, D.; Etsion, Y.; Feitelson, D. G. Backfilling Using System-Generated Predictions Rather than User Runtime Estimates. *IEEE Transactions on Parallel and Distributed Systems* **2007**, *18*, 789–803.

- ¹⁸Gaussier, E.; Glesser, D.; Reis, V.; Trystram, D. Improving backfilling by using machine learning to predict running times. Proceedings of the International Conference for High Performance Computing, Networking, Storage and Analysis on - SC '15. Austin, Texas, 2015; pp 1–10.
- ¹⁹Sonmez, O.; Yigitbasi, N.; Iosup, A.; Epema, D. Trace-based evaluation of job runtime and queue wait time predictions in grids. Proceedings of the 18th ACM international symposium on High performance distributed computing - HPDC '09. Garching, Germany, 2009; p 111.
- ²⁰Li, C. V.; Petrucci, V.; Mosse, D. Predicting Thread Profiles across Core Types via Machine Learning on Heterogeneous Multiprocessors. 2016 VI Brazilian Symposium on Computing Systems Engineering (SBESC). João Pessoa, Paraíba, Brazil, 2016; pp 56–62.
- ²¹Negi, A.; Kumar, P. Applying Machine Learning Techniques to Improve Linux Process Scheduling. TENCON 2005 - 2005 IEEE Region 10 Conference. Melbourne, Australia, 2005; pp 1–6.
- ²²Helmy, T.; Al-Azani, S.; Bin-Obaidellah, O. A Machine Learning-Based Approach to Estimate the CPU-Burst Time for Processes in the Computational Grids. 2015 3rd International Conference on Artificial Intelligence, Modelling and Simulation (AIMS). Kota Kinabalu, Malaysia, 2015; pp 3–8.
- ²³Shulga, D. A.; Kapustin, A. A.; Kozlov, A. A.; Kozyrev, A. A.; Rovnyagin, M. M. The scheduling based on machine learning for heterogeneous CPU/GPU systems. Young Researchers in Electrical & Electronic Engineering Conference. 2016; p 4.
- ²⁴Nadeem, F.; Fahringer, T. Optimizing execution time predictions of scientific workflow applications in the Grid through evolutionary programming. *Future Gener Comput Syst* **2013**, *29*, 926–935.
- ²⁵Singh, K.; İpek, E.; McKee, S. A.; de Supinski, B. R.; Schulz, M.; Caruana, R. Predicting parallel application performance via machine learning approaches. *Concurr Comput* **2007**, *19*, 2219–2235.
- ²⁶Matsunaga, A.; Fortes, J. A. On the Use of Machine Learning to Predict the Time and Resources Consumed by Applications. 2010 10th IEEE/ACM International Conference on Cluster, Cloud and Grid Computing. Melbourne, Australia, 2010; pp 495–504.
- ²⁷Altschul, S. F.; Gish, W.; Miller, W.; Myers, E. W.; Lipman, D. J. Basic local alignment search tool. *J. Mol. Biol.* **1990**, *215*, 403–410.

- ²⁸Stamatakis, A. RAxML version 8: a tool for phylogenetic analysis and post-analysis of large phylogenies. *Bioinformatics* **2014**, *30*, 1312–1313.
- ²⁹Papay, J.; Atherton, T. J.; Zemerly, M. J.; Nudd, G. R. Performance prediction of parallel self consistent field computation. *Parallel Algorithms Appl.* **1996**, *10*, 127–143.
- ³⁰Antony, J.; Rendell, A. P.; Rui, Y.; Trucks, G.; Frisch, M. J. Modelling the Runtime of the Gaussian Computational Chemistry Application and Assessing the Impacts of Microarchitectural Variations. *Procedia Comput. Sci.* **2011**, *4*, 281–291.
- ³¹Mniszewski, S. M.; Junghans, C.; Voter, A. F.; Perez, D.; Eidenbenz, S. J. TADSim: Discrete Event-Based Performance Prediction for Temperature-Accelerated Dynamics. *ACM Trans Model Comput Simul* **2015**, *25*, 1–26.
- ³²Schuld, M.; Sinayskiy, I.; Petruccione, F. An introduction to quantum machine learning. *Contemp. Phys.* **2015**, *56*, 172–185.
- ³³Biamonte, J.; Wittek, P.; Pancotti, N.; Rebentrost, P.; Wiebe, N.; Lloyd, S. Quantum machine learning. *Nature* **2017**, *549*, 195–202.
- ³⁴Ciliberto, C.; Herbster, M.; Ialongo, A. D.; Pontil, M.; Rocchetto, A.; Severini, S.; Wossnig, L. Quantum machine learning: a classical perspective. *Proc. Math. Phys. Eng. Sci.* **2018**, *474*, 20170551, Publisher: Royal Society.
- ³⁵Baerends, E. J.; Gritsenko, O. V. A quantum chemical view of density functional theory. *J. Phys. Chem. A* **1997**, *101*, 5383–5403.
- ³⁶Perdew, J. P.; Ruzsinszky, A.; Tao, J.; Staroverov, V. N.; Scuseria, G. E.; Csonka, G. I. Prescription for the design and selection of density functional approximations: More constraint satisfaction with fewer fits. *J. Chem. Phys.* **2005**, *123*, 062201.
- ³⁷Cohen, A. J.; Mori-Sánchez, P.; Yang, W. Challenges for density functional theory. *Chem. Rev.* **2012**, *112*, 289–320.
- ³⁸Strout, D. L.; Scuseria, G. E. A quantitative study of the scaling properties of the Hartree–Fock method. *J. Chem. Phys.* **1995**, *102*, 8448–8452.
- ³⁹Pérez-Jordá, J. M.; Yang, W. Fast evaluation of the Coulomb energy for electron densities. *J. Chem. Phys.* **1997**, *107*, 1218–1226.
- ⁴⁰Steele, J. M. *The Cauchy-Schwarz master class: an introduction to the art of mathematical inequalities*; Cambridge University Press, 2004.
- ⁴¹Kirkpatrick, P.; Ellis, C. Chemical space. *Nature* **2004**, *432*, 823–823.

- ⁴²Reymond, J.-L.; van Deursen, R.; Blum, L. C.; Ruddigkeit, L. Chemical space as a source for new drugs. *MedChemComm* **2010**, *1*, 30.
- ⁴³Oprea, T. I. Chemical space navigation in lead discovery. *Curr. Opin. Chem. Biol.* **2002**, *6*, 384–389.
- ⁴⁴Oprea, T. I.; Gottfries, J. Chemography: The Art of Navigating in Chemical Space. *J. Comb. Chem.* **2001**, *3*, 157–166.
- ⁴⁵Reymond, J.-L. The Chemical Space Project. *Acc. Chem. Res.* **2015**, *48*, 722–730, Publisher: American Chemical Society.
- ⁴⁶Daniel,; Probst,; Jean-Louis,; Reymond, Exploring Drugbank in Virtual Reality Chemical Space. *J. Chem. Inf. Model.* **2018**, *58*, 1731–1735.
- ⁴⁷Breiman, L. Random Forests. *Mach. Learn.* **2001**, *45*, 5–32.
- ⁴⁸Tin Kam Ho, Random decision forests. Proceedings of 3rd International Conference on Document Analysis and Recognition. 1995; pp 278–282 vol.1.
- ⁴⁹Weininger, D. SMILES, a chemical language and information system. 1. Introduction to methodology and encoding rules. *J. Chem. Inf. Comp. Sci.* **1988**, *28*, 31–36.
- ⁵⁰Weininger, D.; Weininger, A.; Weininger, J. L. SMILES. 2. Algorithm for generation of unique SMILES notation. *J. Chem. Inf. Comp. Sci.* **1989**, *29*, 97–101.
- ⁵¹Weininger, D. SMILES. 3. DEPICT. Graphical depiction of chemical structures. *J. Chem. Inf. Comp. Sci.* **1990**, *30*, 237–243.
- ⁵²Hochreiter, S.; Schmidhuber, J. Long Short-Term Memory. *Neural Comput.* **1997**, *9*, 1735–1780.
- ⁵³Gers, F. A.; Schmidhuber, J.; Cummins, F. Learning to Forget: Continual Prediction with LSTM. *Neural Comput.* **2000**, *12*, 2451–2471.
- ⁵⁴Morgan, D. P.; Scofield, C. L. *Neural Networks and Speech Processing*; Springer US: Boston, MA, 1991; pp 245–288.
- ⁵⁵Graves, A.; Fernández, S.; Schmidhuber, J. Bidirectional LSTM networks for improved phoneme classification and recognition. International Conference on Artificial Neural Networks. 2005; pp 799–804.
- ⁵⁶Sundermeyer, M.; Alkhoul, T.; Wuebker, J.; Ney, H. Translation modeling with bidirectional recurrent neural networks. Proceedings of the 2014 conference on empirical methods in natural language processing (EMNLP). 2014; pp 14–25.

- ⁵⁷Kiperwasser, E.; Goldberg, Y. Simple and accurate dependency parsing using bidirectional LSTM feature representations. *Transactions of the Association for Computational Linguistics* **2016**, *4*, 313–327.
- ⁵⁸Gilmer, J.; Schoenholz, S. S.; Riley, P. F.; Vinyals, O.; Dahl, G. E. Neural Message Passing for Quantum Chemistry. *CoRR* **2017**, *abs/1704.01212*.
- ⁵⁹Lu, C.; Liu, Q.; Wang, C.; Huang, Z.; Lin, P.; He, L. Molecular Property Prediction: A Multilevel Quantum Interactions Modeling Perspective. *Proceedings of the AAAI Conference on Artificial Intelligence* **2019**, *33*, 1052–1060.
- ⁶⁰Everett, H. "Relative State" Formulation of Quantum Mechanics. *Rev. Mod. Phys.* **1957**, *29*, 454–462.
- ⁶¹Everett, H. *The Everett interpretation of quantum mechanics: Collected works 1955-1980 with commentary*; Princeton University Press, 2012.
- ⁶²Wallace, D. *The emergent multiverse: Quantum theory according to the Everett interpretation*; Oxford University Press, 2012.
- ⁶³Tappenden, P. Identity and probability in Everett's multiverse. *Br J Philos Sci* **2000**, *51*, 99–114.
- ⁶⁴Bousso, R.; Susskind, L. Multiverse interpretation of quantum mechanics. *Phys. Rev. D* **2012**, *85*, 045007.
- ⁶⁵Schrödinger, E. Die gegenwärtige Situation in der Quantenmechanik. *Naturwissenschaften* **1935**, *23*, 823–828.
- ⁶⁶Schrödinger, E. Discussion of probability relations between separated systems. *Mathematical Proceedings of the Cambridge Philosophical Society*. 1935; pp 555–563.
- ⁶⁷Einstein, A.; Podolsky, B.; Rosen, N. Can quantum-mechanical description of physical reality be considered complete? *Phys. Rev.* **1935**, *47*, 777.
- ⁶⁸Yin, J.; Cao, Y.; Yong, H.-L.; Ren, J.-G.; Liang, H.; Liao, S.-K.; Zhou, F.; Liu, C.; Wu, Y.-P.; Pan, G.-S., et al. Lower bound on the speed of nonlocal correlations without locality and measurement choice loopholes. *Phys. Rev. Lett.* **2013**, *110*, 260407.
- ⁶⁹Perdew, J. P.; Schmidt, K. Jacob's ladder of density functional approximations for the exchange-correlation energy. *AIP Conference Proceedings*. 2001; pp 1–20.
- ⁷⁰Moulton, R.; Jiang, Y. Maximally Consistent Sampling and the Jaccard Index of Probability Distributions. *IEEE International Conference on Data Mining, ICDM 2018, Singapore, November 17-20, 2018*. 2018; pp 347–356.

- ⁷¹Levandowsky, M.; Winter, D. Distance between sets. *Nature* **1971**, 234, 34–35.
- ⁷²Jaccard, P. Étude comparative de la distribution florale dans une portion des Alpes et des Jura. *Bull. Soc. Vaudoise Sci. Nat.* **1901**, 37, 547–579.
- ⁷³Pritchard, B. P.; Altarawy, D.; Didier, B. T.; Gibson, T. D.; Windus, T. L. A New Basis Set Exchange: An Open, Up-to-date Resource for the Molecular Sciences Community. *J. Chem. Inf. Model.* **2019**,
- ⁷⁴Turcani, L.; Berardo, E.; Jelfs, K. STK: A Python Toolkit for Supramolecular Assembly. **2018**,
- ⁷⁵The RDKit Documentation — The RDKit 2019.03.1 documentation. <http://www.rdkit.org/docs/index.html>.
- ⁷⁶Frisch, M. J. et al. Gaussian09 Revision D.01. Gaussian Inc. Wallingford CT 2009.
- ⁷⁷Apra, E.; Bylaska, E. J.; De Jong, W. A.; Govind, N.; Kowalski, K.; Straatsma, T. P.; Valiev, M.; van Dam, H. J.; Alexeev, Y.; Anchell, J., et al. NWChem: Past, present, and future. *J. Chem. Phys.* **2020**, 152, 184102.
- ⁷⁸Barca, G. M. J. et al. Recent developments in the general atomic and molecular electronic structure system. *J. Chem. Phys.* **2020**, 152, 154102.
- ⁷⁹Fdez. Galván, I.; Vacher, M.; Alavi, A.; Angeli, C.; Aquilante, F.; Autschbach, J.; Bao, J. J.; Bokarev, S. I.; Bogdanov, N. A.; Carlson, R. K., et al. OpenMolcas: From source code to insight. *J. Chem. Theory Comput.* **2019**, 15, 5925–5964.
- ⁸⁰Paszke, A.; Gross, S.; Chintala, S.; Chanan, G.; Yang, E.; DeVito, Z.; Lin, Z.; Desmaison, A.; Antiga, L.; Lerer, A. Automatic differentiation in PyTorch. **2017**,
- ⁸¹Wishart, D. S.; Knox, C.; Guo, A. C.; Shrivastava, S.; Hassanali, M.; Stothard, P.; Chang, Z.; Woolsey, J. DrugBank: a comprehensive resource for in silico drug discovery and exploration. *Nucleic Acids Res.* **2006**, 34, D668–D672.
- ⁸²Wishart, D. S.; Knox, C.; Guo, A. C.; Cheng, D.; Shrivastava, S.; Tzur, D.; Gautam, B.; Hassanali, M. DrugBank: a knowledgebase for drugs, drug actions and drug targets. *Nucleic Acids Res.* **2008**, 36, D901–D906.
- ⁸³Law, V.; Knox, C.; Djoumbou, Y.; Jewison, T.; Guo, A. C.; Liu, Y.; Maciejewski, A.; Arndt, D.; Wilson, M.; Neveu, V., et al. DrugBank 4.0: shedding new light on drug metabolism. *Nucleic Acids Res.* **2014**, 42, D1091–D1097.
- ⁸⁴Kingma, D.; Ba, J. Adam: A Method for Stochastic Optimization. *Comput. Sci.* **2014**, Publisher: arXiv.

- ⁸⁵Ditchfield, R.; Hehre, W. J.; Pople, J. A. Self-consistent molecular-orbital methods. IX. An extended Gaussian-type basis for molecular-orbital studies of organic molecules. *J. Chem. Phys.* **1971**, *54*, 724–728.
- ⁸⁶Zhao, Y.; Truhlar, D. G. The M06 suite of density functionals for main group thermochemistry, thermochemical kinetics, noncovalent interactions, excited states, and transition elements: two new functionals and systematic testing of four M06-class functionals and 12 other functionals. *Theor. Chem. Acc.* **2008**, *120*, 215–241.
- ⁸⁷Perdew, J. P.; Burke, K.; Ernzerhof, M. Generalized gradient approximation made simple. *Phys. Rev. Lett.* **1996**, *77*, 3865.
- ⁸⁸Becke, A. D. Density-functional exchange-energy approximation with correct asymptotic behavior. *Phys. Rev. A* **1988**, *38*, 3098.
- ⁸⁹Lee, C.; Yang, W.; Parr, R. G. Development of the Colle-Salvetti correlation-energy formula into a functional of the electron density. *Phys. Rev. B* **1988**, *37*, 785.
- ⁹⁰Becke, A. D. A new mixing of Hartree–Fock and local density-functional theories. *J. Chem. Phys.* **1993**, *98*, 1372–1377.
- ⁹¹Raghavachari, K. Perspective on “Density functional thermochemistry. III. The role of exact exchange”. *Theor. Chem. Acc.* **2000**, *103*, 361–363.
- ⁹²Iikura, H.; Tsuneda, T.; Yanai, T.; Hirao, K. A long-range correction scheme for generalized-gradient-approximation exchange functionals. *J. Chem. Phys.* **2001**, *115*, 3540–3544.
- ⁹³Yanai, T.; Tew, D. P.; Handy, N. C. A new hybrid exchange–correlation functional using the Coulomb-attenuating method (CAM-B3LYP). *Chem. Phys. Lett.* **2004**, *393*, 51–57.
- ⁹⁴Chai, J.-D.; Head-Gordon, M. Long-range corrected hybrid density functionals with damped atom–atom dispersion corrections. *Phys. Chem. Chem. Phys.* **2008**, *10*, 6615–6620.
- ⁹⁵Schäfer, A.; Horn, H.; Ahlrichs, R. Fully optimized contracted Gaussian basis sets for atoms Li to Kr. *J. Chem. Phys.* **1992**, *97*, 2571–2577.
- ⁹⁶Dunning Jr, T. H. Gaussian basis sets for use in correlated molecular calculations. I. The atoms boron through neon and hydrogen. *J. Chem. Phys.* **1989**, *90*, 1007–1023.
- ⁹⁷Zhang, D. W.; Zhang, J. Molecular fractionation with conjugate caps for full quantum mechanical calculation of protein–molecule interaction energy. *J. Chem. Phys.* **2003**, *119*, 3599–3605.

- ⁹⁸He, X.; Zhang, J. Z. The generalized molecular fractionation with conjugate caps/-molecular mechanics method for direct calculation of protein energy. *J. Chem. Phys.* **2006**, *124*, 184703.
- ⁹⁹Zhang, B.; Ma, Y.; Jin, X.; Wang, Y.; Suo, B.; He, X.; Jin, Z. GridMol2. 0: Implementation and application of linear-scale quantum mechanics methods and molecular visualization. *Int. J. Quantum Chem.* **2020**, e26402.
- ¹⁰⁰Al Hajj, M.; Malrieu, J.-P.; Guihéry, N. Renormalized excitonic method in terms of block excitations: Application to spin lattices. *Phys. Rev. B* **2005**, *72*, 224412.
- ¹⁰¹Ma, Y.; Liu, Y.; Ma, H. A new fragment-based approach for calculating electronic excitation energies of large systems. *J. Chem. Phys.* **2012**, *136*, 024113.
- ¹⁰²Ma, Y.; Ma, H. Calculating excited states of molecular aggregates by the renormalized excitonic method. *J. Phys. Chem. A* **2013**, *117*, 3655–3665.
- ¹⁰³Pedregosa, F. et al. Scikit-learn: machine learning in Python. *J. machine learning Res.* **2011**, *12*, 2825–2830.
- ¹⁰⁴Zhou, P.; Shi, W.; Tian, J.; Qi, Z.; Li, B.; Hao, H.; Xu, B. Attention-Based Bidirectional Long Short-Term Memory Networks for Relation Classification. Proceedings of the 54th Annual Meeting of the Association for Computational Linguistics (Volume 2: Short Papers). Berlin, Germany, 2016; pp 207–212.
- ¹⁰⁵Cho, K.; Van Merriënboer, B.; Bahdanau, D.; Bengio, Y. On the properties of neural machine translation: Encoder-decoder approaches. *arXiv preprint arXiv:1409.1259* **2014**,
- ¹⁰⁶Vinyals, O.; Bengio, S.; Kudlur, M. Order Matters: Sequence to sequence for sets. *CoRR* **2015**, *abs/1511.06391*.
- ¹⁰⁷Broomhead, D. S.; Lowe, D. *Radial basis functions, multi-variable functional interpolation and adaptive networks*; 1988.
- ¹⁰⁸Schwenker, F.; Kestler, H. A.; Palm, G. Three learning phases for radial-basis-function networks. *Neural Netw.* **2001**, *14*, 439–458.